2020

Supercritical CO2 Heat Transfer Study Near Critical Point in a Heated Circular Pipe

Akshay Khadse
University of Central Florida

SUPERCRITICAL CO_2 HEAT TRANSFER STUDY NEAR CRITICAL POINT IN A HEATED CIRCULAR TUBE

by

AKSHAY KHADSE
B.Tech. Aerospace Engineering, IIT Bombay, 2015
M.Tech. Aerospace Engineering, IIT Bombay, 2015

A dissertation submitted in partial fulfillment of the requirements
for the degree of Doctor of Philosophy
in the Department of Mechanical and Aerospace Engineering
in the College of Engineering and Computer Science
at the University of Central Florida
Orlando, Florida

Spring Term
2020

Major Professor: Jayanta S. Kapat

ABSTRACT

Supercritical CO_2 (sCO_2) power cycle is an up-and-coming technology to produce electricity from various heat sources. Apart from power cycles, sCO_2 can also be used as coolant in centralized cooling system and stand-alone cooling device. However, lack of accurate predication tools such as heat transfer coefficient correlations and insufficient knowledge behind fundamental heat transfer processes can hinder its practical realization in key energy and cooling systems. The overall objective of the study is to extend fundamental knowledge about heat transfer and fluid flow processes in conduits pertinent to sCO_2 power cycle. The emphasis here is investigation of heat transfer effects of three testing parameters: heat flux, inlet mass flux and inlet temperature. Experimental setup for this heat transfer study is designed considering limitations due to high pressure rating requirements and thus follows unconventional approach to calculate heat transfer coefficient. Test section chosen is a horizontal stainless steel tubing of inner diameter of 9.4 mm and heated length of 1.23 m with uniform volumetric heat generation within tubing walls. The designed test apparatus and data reduction process are validated with high pressure air experiments. Nusselt numbers are calculated at top, bottom and sidewall locations to demonstrate effects of buoyancy. Enhancement of heat transfer at bottom wall surfaces and deterioration at top wall surfaces is observed as the main effect of buoyancy. It was observed that effects of buoyancy increase with heat flux and decrease with mass flux. Buoyancy effects are also decreased for fluid temperatures higher than pseudocritical temperature. Nusselt numbers calculated from experimental results are compared with Nusselt number from available correlations in literature. It is hinted that near critical region where property variations are significant, one correlation alone may not accurately predict heat transfer for different regimes of geometry, mass flux and heat flux.

Dedicated to my mother, Lalita and my brother, Chetan. This dissertation and resulting doctoral degree is a symbol of what we have achieved as a family. This one is for us!

ACKNOWLEDGMENTS

First and most of all, I would like to express my gratitude to my advisor and mentor Dr. Jayanta Kapat for his guidance, motivation and endless support throughout my time at UCF. Without your guidance and support, this research would not have been completed. I will forever be in debt to your priceless advice.

Also, I would like to extend my gratefulness to my committee members. The help and support from Dr. Vasu, Dr. Gou and Dr. Blair significantly improved the quality of my research and this dissertation through their constant feedback. Alongside my committee, I would like to thank CATER and IST for their resources and great people.

To my labmates Andres, Alok, Gaurav, Husam, Ian, James, Jorge, Justin, Kevin, Ladislav, Luisana, Marcel, Nandhini, Patrick, Shinjan, Vipul and Wilmer thank you for the education, support and fun.

Thank you to all of the many great people that I have met during my time at UCF. Especially, my friends Divyasree, Dushyant, Hari, Harini, Pankaj, Quana, Saurabh, Urvik and Vibhav, who always made me feel I am at home when I am with them.

I would also like to thank UCF Table Tennis Team for giving me opportunity to pursue my hobby and have a wonderful time outside my lab. I will always cherish our moments of joy, excitement and comradeship during USA National Collegiate Tournaments and our weekly practices.

Lastly, I would not be here without the support of my mother Lalita and brother Chetan. Thank you for constantly serving as a support system and source of my motivation.

TABLE OF CONTENTS

LIST OF FIGURES

LIST OF TABLES

NOMENCLATURE

$\overline{c}_p$	$\overline{c}_p = \frac{h_w - h_b}{T_w - T_b}$
A	Area$[m^2]$
D	Diameter$[m]$
g	Acceleration due to gravity$[m/s^2]$
h	Enthalpy $[J/kg]$
HTC	Heat Transfer Coefficient$[W/m^2.K]$
I	Current$[A]$
k	Thermal conductivity$[W/m.K]$
kWe	kilowatt electric
L	Length$[m]$
P	Pressure $[Pa]$
q	Heat flow rate$[W]$
r	Radius$[m]$
RC	Recuperated cycle
Re	Reynolds Number
RRC	Recuperated recompression cycle

T Temperature $[K]$

U Equivalent heat transfer coefficient$[W/m^2.K]$

V Voltage$[V]$

Greek Symbols

β Thermal expansion coefficient

μ Dynamic viscosity$[Pa.s]$

ρ Density$[kg/m^3]$

Dimensionless numbers

$\overline{Pr}_b$ $\overline{Pr}_b = \mu_b \bar{c}_p / k_b$

Bu_j Jackson buoyancy parameter

cs cross-section of tubing

Gr Grashof number

$LMTD$ Log Mean Temperature Difference

Nu Nusselt number

Pr Prandtl number

Re Reynolds number

Ri Richardson number

y^+ Non-dimensional wall distance

Superscripts and Subscripts

amb Ambient

ave Average

$b, bulk$ Bulk flow property

c cross section of tube

CFD Computational fluid dynamics

cir in circular direction

$cond$ conduction heat transfer

DB using Dittus-Boelter correlation

$Exp, expt$ Experimental

ext at external wall

Gn using Gnielinski correlation

i index for location of the node

$inlet$ Inlet of the test section

int at internal wall

$local$ calculated for local heated test section

SS Stainless Steel

$total$ calculated for total heated test section

vl Volumetric

$w, wall$ At wall

CHAPTER 1: INTRODUCTION

Supercritical CO_2 Power Cycles

As observed for several past decades, electricity will remain the main form of worldwide energy through 2040 [2]. For future electricity needs, links among thermodynamic, economic, and environmental analysis of energy conversion system become very important. With the current increasing demand of electricity, and the knowledge that natural gas is one of the leading providers, it is essential to develop means to efficiently convert heat into electricity. One of the way researchers are attempting to meet the world's energy needs is by exploring alternative working fluids in power generation cycles, such as supercritical carbon dioxide (sCO_2), that show potential to enhance cycle efficiency while lowering the capital cost and output pollution. The ability of sCO_2 Brayton cycles to operate in a range of temperatures makes this cycle applicable in multiple power generation environments as the power conversion option. Some potential applications include concentrated solar power systems (CSP), nuclear reactors, and waste heat recovery. Use of supercritical CO_2 (sCO_2) as a working fluid allows efficient conversion of waste heat from industrial processes to electricity, or economic and automatic carbon capture in use of natural gas for power generation. In fact, sCO_2 power cycle technology has been touted as the "Green Fossil Fuel" [3] technology for this reason. In addition, because of unique properties of sCO_2, the turbomachinery needed for such power cycles can be very compact, thus leading to cost savings for such systems. Turchi et al. has studied sCO_2 Brayton cycles for application of CSP extensively and explains the advantages of sCO_2 power cycles when compared to steam cycles. The study included more simple plant design compared to Rankine cycles along with higher efficiencies, and smaller size and volume due to the high density of carbon dioxide at the specified operating condi-

tions. sCO_2 power cycles present promising potential for next generation power cycles. sCO_2 cycles require relatively low power for compression with inlet operating conditions close to the fluid's critical point, T=304.13 K and P=7.69 MPa [4]. For sCO_2 Brayton cycles, 25-30% of the gross power produced from the turbine is usually spent to operate the compressor versus the usual 45% or so of other current working fluids such as helium, its competitor in nuclear reactor systems [4]. As a result, it has been observed that the amount of research being performed on the possible cycle configuration and optimization is expanding. Turchi et al. [5] and Mohagheghi and Kapat [6] studied different cycle configurations and optimization tools to assess the most practical power cycle designs for solar tower applications. Dostal et al. [7] presents a significant decrease in the turbine size and system complexity for sCO_2 power cycles when compared to helium and steam power cycles.

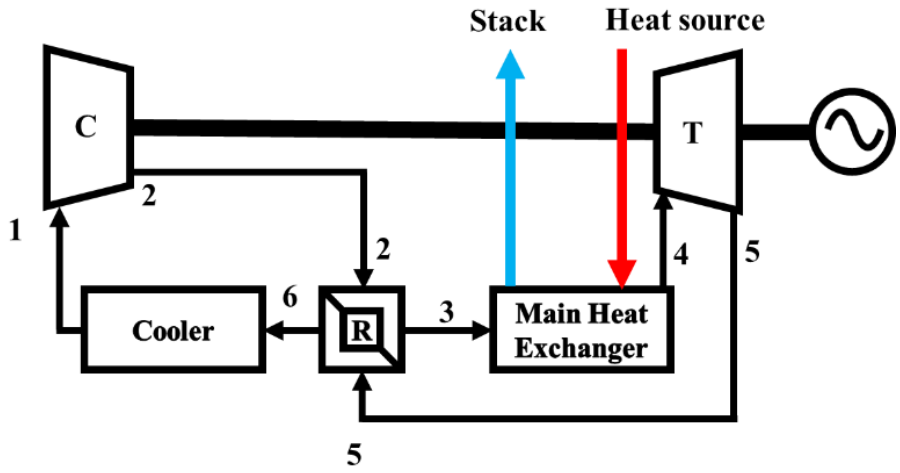

Figure 1.1: Recuperated configuration of Brayton cycle

Two of the most studied configurations of sCO_2 Brayton cycles are: 1) Recuperated cycle (RC) shown in Figure 1.1 and 2) Recuperated recompression cycle (RRC) shown in Figure 1.2.

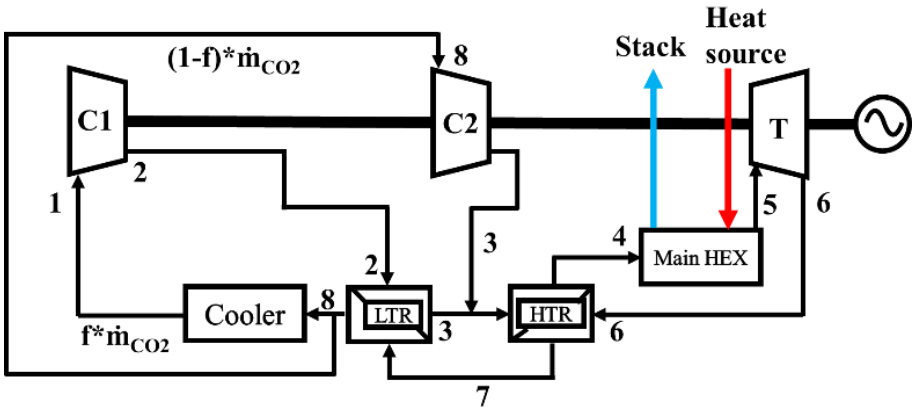

Figure 1.2: Recuperated recompression configuration of Brayton cycle

Table 1.1: Net capital cost for the optimized RRC cycle [1]

Component	**Cost (2017 k$)**
HT recuperator	9994
LT recuperator	8293
Precooler	6870
Main heat exchanger	18,323
Turbomachinery	19,576
Total direct cost	63,056
Total indirect cost	31,528
Total capital cost for RRC	94,584

Capital cost per kWe, RRC	**860**
Capital cost per kWe, Steam	**1,200**

In a thermodynamic optimization study [1], both RC and RRC configurations were studied to find out which suits better for heat recovery from exhaust of SGT6-8000H gas turbine [8]. It was reported that for the chosen heat source, RRC configuration yields more power output (110 MW) compared to RC configuration (90 MW). Further capital cost analysis of the RRC cycle ($860/kWe) showed 28% reduction compared to steam alternative($1200/kWe, [9]). The capital cost breakdown of the RRC cycle is listed in

Table 1.1. This proves that sCO_2 cycles can be a viable option for waste heat recovery replacing steam. Table 1.2 lists existing and ongoing sCO_2 demo powerplants.

Table 1.2: List of existing and ongoing sCO_2 demo powerplants

Name	**Capacity**	**Heat source**	**Location**	**Status**
Echogen EPS 100 [10]	8 MWe	Indirect heating	Portable generator	Successful demo
NET Power [11]	25 MWe	Natural gas direct combustion heating	La Porte, TX, USA	Successful demo
Sunshot [12]	10 MWe	Concentrated Solar Power	San Antanio, TX, USA	Successful demo
NET Power [11]	300 MW	Natural gas direct combustion heating	La Porte, TX, USA	In progress
STEP [13]	10 Mwe	Natural gas/Coal indirect heating	San Antanio, TX, USA	In progress

Heat Transfer in Supercritical CO_2 Flows

sCO_2 cycles are highly recuperative in nature. Good amount of heat addition to sCO_2 comes from recuperative heat exchangers. Performance of recuperators as well as the main heat exchanger in case of indirect cycle, obviously affect net cycle output. For better performance out of these heat exchangers, high surface area-to-volume ratio is preferred. However, because of high surface area-to-volume ratio, cost of these heat exchangers is also very high. For example, in previous study on cycle optimization [1], the cost of heat exchangers amounted 69% (Figure 1.3) of overall direct capital cost. Hence, optimized design of heat exchangers is very important from not only performance but also financial point of view. Sound and reliable design of such heat exchangers require accurate heat transfer correlations. However, there are still gaps in the knowledge of heat transfer of sCO_2 flows. Heat transfer in sCO_2 flows is highly related to length scale effects. Different mechanisms dominate the heat transfer process at different length scales

and operating conditions, such as viscous effects especially at the small length scale spectrum, which inhibit flow mixing, and buoyancy effects at the bigger length scales.

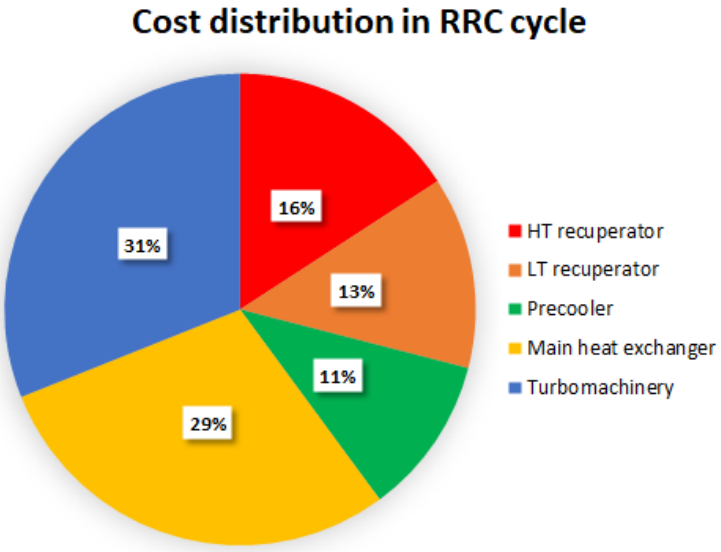

Figure 1.3: Cost distribution in RRC cycle plotted from cycle optimization study [1] showing cost of heat exchangers as majority

The proximity to the critical point that provides key advantages to sCO_2 power cycles and cooling systems creates challenges because of considerable fluctuations in thermal and fluid properties close to the critical point. Spikes and drastic variations in thermophysical properties near critical point for CO_2 can be seen in Figure 1.4. Under these conditions, the nature of the flow and heat transfer processes, and hence heat transfer coefficient and friction factor, can vary considerably. However, the fluid mechanics and thermal transport are not well understood when the fluid property distributions, such as specific heat, thermal conductivity, viscosity, and density are highly non-linear as the fluid temperature changes inside the boundary layers. These processes vary appreciably depending on the flow conditions (e.g., Reynolds number, Grashof number, Prandtl number, etc.) and thermal conditions (e.g., heat flux, inlet fluid temperature). No conven-

tional, established correlations are meant for such severe variations in fluid properties. However, available correlations for sCO_2 are inconsistent and are unable to reveal the nature of fluid flow and heat transfer close to the wall. The performance of heat exchanger for regeneration at the low temperature end is quite critical for overall performance of sCO_2 power cycle, as this end contains the pinch point and hence the limitations to heat transfer.

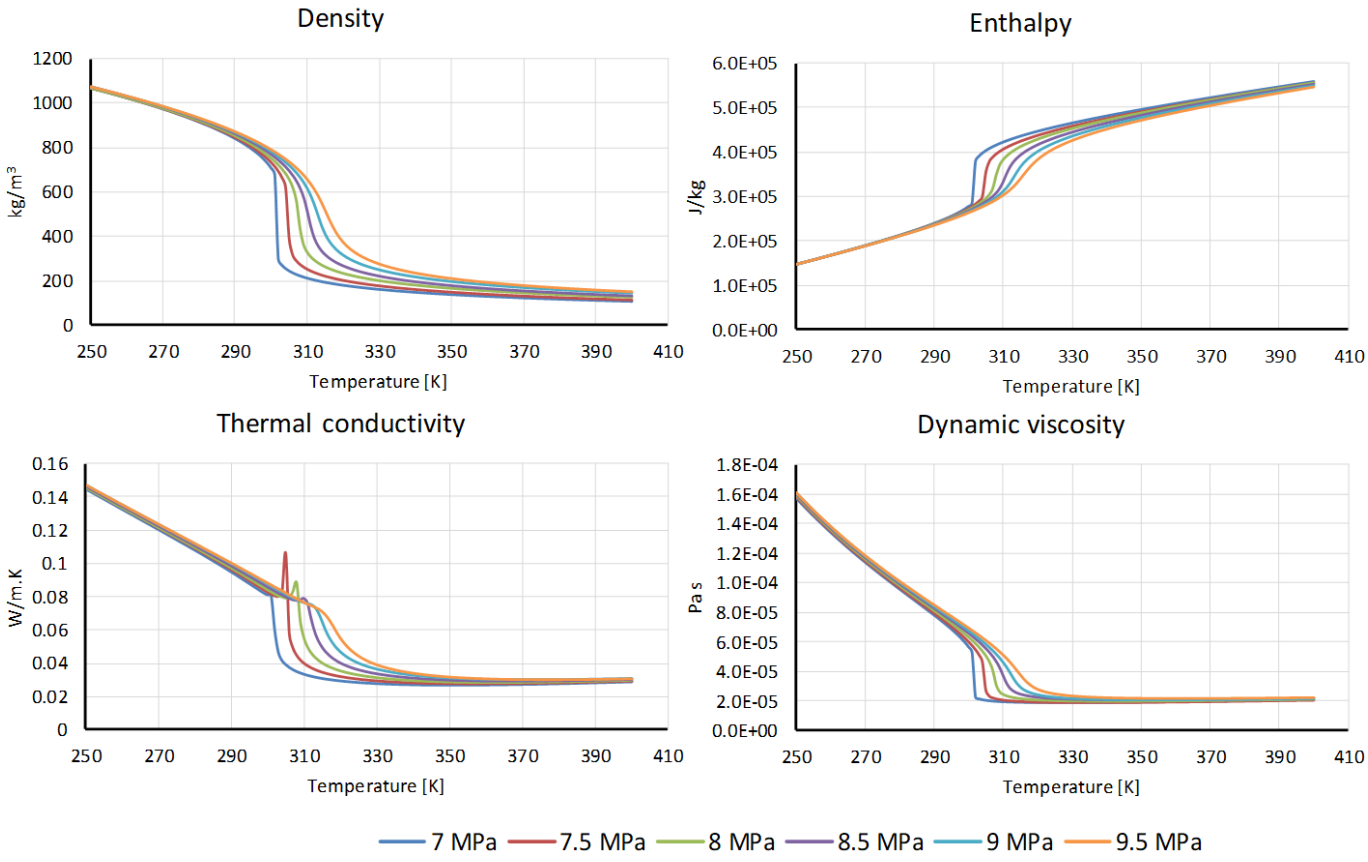

Figure 1.4: CO_2 property isobars near critical pressure

Accurately predicting the heat transfer of CO_2 at supercritical pressure within pipes of varying diameters is important to ensure the reliability under different condi-

tions. It has been reported that for channel flows, density and thermal conductivity variation can create buoyancy effects [14–25]. Source of this buoyancy effect is the high density gradient between wall and bulk fluid due to high temperature difference between wall and bulk fluid. Since buoyancy-driven heat transfer processes have strong dependence on relevant linear dimension, there can be size effect regarding how strongly buoyancy can play a role in sCO_2 heat transfer. This requires study with a range of channel cross-sectional dimensions. In addition, orientation of flow channels will play a role as well.

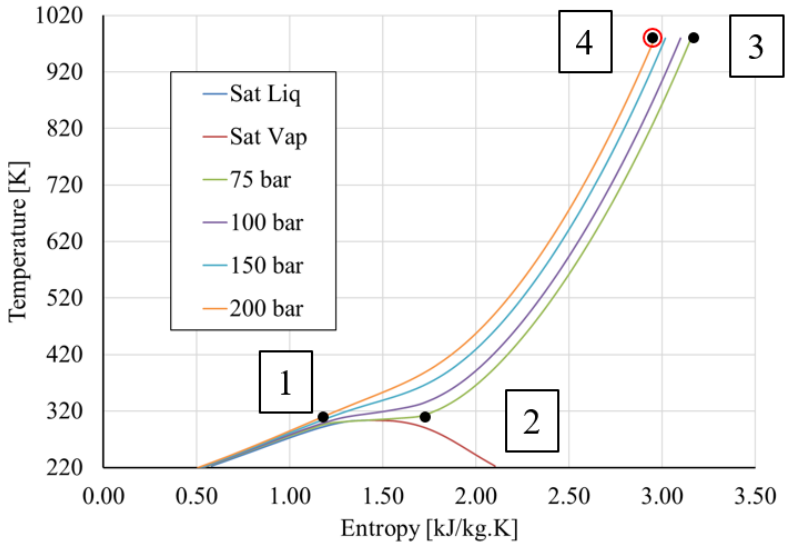

Figure 1.5: Temperature-Entropy diagram for CO_2 (1, 2, 3, 4 are four states, not necessarily corresponding to a thermodynamic cycle)

In this dissertation, effects of buoyancy on sCO_2 heat transfer are explained with the help of experimental data near critical region. Deshmukh et. al. [26] reported that for air cooler in sCO_2 Brayton cycle, pinch point can move from one position to another. Hence better understanding of heat transfer of CO_2 is very important since transients in air cooler affects compressor in the power cycle directly. This region is around conditions

1 and 2 in Figure 1.5 on T-s diagram of CO_2. It is important to note that at conditions 3 and 4, the compressibility factor is very close to 1 while at conditions 1 and 2 it is 0.51 and 0.4 respectively. This hints at stronger effect of property variation on heat transfer near states 1 and 2. For this dissertation, experiments were conducted with uniform heat flux at tubing wall. The experimental setup built for this purpose has capability to test very high temperatures (538^{o}C) and high pressure (20 MPa). Because of such capabilities, experiments can be conducted away from the critical point to investigate at which conditions the sCO_2 heat transfer starts to become more predictable and similar to conventional forced convection heat transfer. However, this dissertation discusses sCO_2 heat transfer results near critical point. Results with horizontal test section with a single internal pipe diameter are reported here. Testing away from critical point, with different size test section at different inclinations will be the focus of future studies.

CHAPTER 2: LITERATURE REVIEW

CO_2 is not the only supercritical working fluid studied for power cycles. Water and helium were also part of the research focus during 1950-70 [27]. The main objective was development of design of supercritical steam generators and water-cooled nuclear reactors. sCO_2 was primarily studied during that time to model supercritical water since CO_2 has lower critical temperature and pressure. This same advantage of lower critical parameters lead researchers to choose CO_2 as working fluid for supercritical power cycles during early 2000s.

There is abundant literature available for heat transfer to sCO_2 beginning from 1960s with different inlet parameters, inclination and pipe sizes. For this dissertation, studies focused on effects of buoyancy in horizontal circular pipes are selected. Effect of buoyancy is best understood by observing circumferential density variation at a cross section. When density at the wall surfaces is significantly lower than the bulk flow density, effects of buoyancy are observed. In horizontal flow configuration, this low density CO_2 rises from the bottom wall to the top wall. This convective movement increases heat transfer rate at the bottom surface. This results in higher temperature at the top wall and lower temperature at the bottom wall.

Adebiyi and Hall [17] and Jackson [23] are early studies which observed this effect of buoyancy. Prior to them, many researchers studied heat transfer in horizontal circular pipes [28–32]. Even though Schnurr [31] reported difference between top and bottom wall temperatures, the word 'buoyancy' was not used to explain what exactly was causing this circumferential variation. As discussed earlier, size of the pipe plays important role in deciding whether buoyant flows will occur or not. Grashof number which is considered the ratio of the buoyancy to viscous forces acting on a fluid is proportional to third power of characteristic length. Liao and Zhao reported significant buoyancy effects for tubes with

diameter larger than 2 mm compared to smaller size tubes. Jackson [23] reported a new form of Grashof number based on bulk fluid properties and properties at the wall (Equation 2.1). Based on this Grashof number, Jackson proposed a new buoyancy parameter as shown in Equation 2.2. For Bu_j < 10, buoyancy effects are negligible.

$$Grashof\ number,\ Gr = \frac{(\rho_w - \rho_b)\ \rho_b\ g\ d^3}{\mu_b^2} \tag{2.1}$$

$$Bu_j = \frac{Gr}{Re_b^2}\frac{x^2}{D^2}\frac{\rho_b}{\rho_w} \tag{2.2}$$

Adebiyi and Hall [17] conducted heat transfer experiments for horizontal flows in 22.1 mm tube 7.6 Mpa. They reported non-uniform circumferential profile. The bottom surface experienced enhanced heat transfer while the heat transfer on top surface was lower than buoyancy free forced convection. For all of their experimental cases, the value of Bu_j was greater than 400, satisfying the criterion for onset of buoyancy. They also mention that even though the results are consistent with the buoyancy criterion, it "cannot be regarded as a stringent test of it".

Pidaparti et. al. [18] performed systematic experiments to investigate buoyancy effects on heat transfer. They included different test variables such as heat flux, testing pressure, mass flux and flow inclination. They reported enhanced heat transfer for downward flow and reduced heat transfer for upward flow. This is mainly because of enhancement and deterioration of turbulent shear stress due to buoyancy in downward and upward flow, respectively. For horizontal flows, top surfaces experienced higher temperature than the bottom surface of the tube. This is the characteristic of buoyancy driven heat transfer. For horizontal flows, Bu_j performed well as onset criterion for buoyancy. They also suggested that when bulk flow temperature is lower than pseudocritical temperature, buoyancy effects are observed for all three flow inclinations. Pseudocritical

temperature at a pressure is the value of temperature where thermophysical properties show peaks for that value of pressure. It is defined as follows:

$$Tpsc = -122.6 + 6.124P - 0.1657P^2 + 0.01773P^{2.5} - 0.0005608P^3 \tag{2.3}$$

Tanimizu and Sadr [33] conducted heat transfer experiments for circular horizontal pipe of size 8.7 mm. They also reported heat transfer enhancement for bottom wall surface and deterioration for top wall surface. They utilized modified Richardson number, Bu_j and buoyancy parameter suggested by Petukhov et. al. [34] to correlate to the enhancement and deterioration due to buoyancy. However, they concluded that, even though all these parameters perform well as a threshold criterion, they do not agree with the variations and magnitude of heat transfer enhancement and deterioration. This hinted towards need of new buoyancy parameter which can not only predict onset of buoyancy but also predict trend and magnitude of enhancement and deterioration of heat transfer due to buoyancy.

Table 2.1: List of previous studies on buoyancy effects on supercritical CO_2 heat transfer

Reference	**P**	**T**	**Heat flux**	**Mass flux**	**Pipe diameter**
	[MPa]	**[^{o}C]**	**[kW/m^2]**	**[kg/m^{2}s]**	**[mm]**
Adebiyi and Hall	7.6	10-31	5-40	m = 0.035-0.15 kg/s	22.1
Pidaparti et. al.	7.5, 8.1 and 10.2	20-55	10-65	150-350	10.9
Tanimizu and Sadr	7.5-9.0	24-28	16-64	m= 0.011-0.017 kg/s	8.7
Kim et. al.	7.6-7.7	30	3.1-25.9	64.1-250.5	7.75
This study	**7.4-7.5**	**30-60**	**2.7-11.8**	**50-80**	**9.4**

For further investigation of validity of these buoyancy parameter, Kim et. al. [22], performed heat transfer experiments for 7.75 mm horizontal tube with different heat flux and mass flux. Even though the buoyancy effects are observed, they came to the same conclusion as Tanimizu and Sadr [33] that the available buoyancy parameters should only

be used as threshold or onset of buoyancy and should not be used to predict trend and amount of enhancement and deterioration.

Summary

Study of heat transfer to supercritical fluids started from 1950s to develop and design supercritical steam generators and supercritical water-cooled nuclear reactors [27]. Even though in early days, carbon dioxide was only used to model supercritical water, in early 2000s, researchers started looking into sCO_2 power cycles as viable alternative to produce electricity. Variation of heat transfer within a cross-section in case of horizontal flow due to effects of buoyancy is studied by a few researchers. The key observation in horizontal flow is enhancement of heat transfer at bottom surface of pipe and deterioration of heat transfer at top wall of the pipe. Parameters to predict this buoyancy effect perform very well to estimate onset of buoyancy but fail to estimate trends and magnitude of heat transfer enhancement and deterioration.

The study presented in this dissertation aims to further investigate validity of the buoyancy parameters as well as discuss trends in supercritical heat transfer for circular horizontal pipe.

CHAPTER 3: OBJECTIVE AND MOTIVIATION

Objective of the Present Study

Heat transfer and heat recuperation are very critical for any sCO_2 cycle. For indirect closed loop cycles, work output of cycle is directly proportional to the heat exchanged from primary heat source to the sCO_2 loop. This means that the performance main heat exchanger will explicitly decide cycle work output. As shown by Mohagheghi and Kapat [6] in their work on sCO_2 Brayton power cycles, the amount of recuperative heat exchange which occurs close to the critical point is about 2.5 times larger than the heat input and about 4.5 times larger than the net power output of the cycle. Figure 1.3 also suggest importance of heat exchanger from financial point of view. These numbers show the importance of recuperators and heat exchangers in sCO_2 cycles, and hence the importance of having accurate understanding of the heat transfer process inside the heat exchangers. This leads to the motivation of this study.

Novelty

Novelty of the study lies in the experimental setup to study heat transfer. Uniqueness and peculiarities of sCO_2 flow and heat transfer, especially those for components of DOE-funded STEP facility, have led to establishing a unique testing facility at UCF, under the sponsorship of NETL, which will be utilized for the validation of internal or sCO_2-side heat transfer in this project. This rig is designed for studying heat transfer characteristics of sCO_2 at high pressure (27MPa) and high temperature (700^oC). The rig has capabilities of heat transfer testing of sCO_2 through stainless steel and Inconel tubing of different diameters. Because of high pressure rating at high temperature, some heat transfer measurement techniques cannot be applied. For example, segmented heated copper-blocks

with embedded thermocouples to give module-averaged heat transfer co- efficient cannot be used since any type of segmentation will void the pressure rating. Local measurements with paints, over a thick insulating substrate, where paint indicate change of temp through some type of optical access cannot be done either. Since the heating is done by providing electricity to the metal tubing, the tubing cannot have any machining done for optical window access. It is not possible to create pressure taps for local pressure measurements as this machining will cause non-uniformity in heat flux. Hence for the current testing, seamless stainless-steel tubing with outside wall temperature measurements is utilized. Pressure de-rating of stainless steel at temperatures higher than 500^{o}C is also taken into consideration while designing the setup. For temperatures higher than 538^{o}C (1000^{o}F), Inconel tubing will be used in the test section instead of stainless-steel tubing. Since the heating is provide by passing electricity through the test section tubing, it is important to insulate the test section from rest of the loop to create additional current circuit. Hence the test section is insulated from rest of the loop using custom-design high temperature dielectric flanges.

Intellectual Contribution and Research Impact

The intellectual merit of this dissertation would be providing insight into heat transfer for supercritical and near critical state of sCO_2 which will help in design of heat exchangers for sCO_2 power cycles. Difference in temperature of bulk flow and temperature at wall can cause significant density variation across circumference which can lead to buoyancy effects on heat transfer. Recent results from an ongoing DOE/NETL funded project at UCF show that near critical point region, sCO_2 flows can exhibit as much as factor-of-4 deviation in heat transfer coefficient from the established correlations for heat transfer coefficients. Moreover, because of significant variations in fluid density of sCO_2

in the same pipe cross-section, buoyancy-induced circulations can cause significant (as much as $\times$ 2.5) variation in heat transfer coefficients circumferentially around the tube.

In summary, this study provides detailed insight into sCO_2 heat transfer for following conditions:

- Validated experimental setup to study sCO_2 heat transfer
- Near critical point heat transfer in horizontal circular tube
- Effects of heat flux and mass flux on sCO_2 heat transfer
- Effect of bulk temperature due to vicinity to pseudocritical temperature on heat transfer

CHAPTER 4: EXPERIMENTAL SETUP

The heat transfer measurement is sensitive to ambient conditions, measuring procedures and measuring instruments. The design of the experimental loop as well as the test section depends highly on required pressure and temperature rating. Concurrently, validation of heat transfer, uncertainty analysis and heat loss are important to establish reliability in the setup. This chapter discusses description of the experimental loop, instrumentation of the test section, uncertainty analysis, heat loss tests, data reduction and validation with high pressure air experiments.

Rationale behind experimental approach

Experimental loop for this study is designed considering high pressure (200 bar) and high temperature (540^{o}C) operating conditions for future testing. For safe operation at such extreme conditions, ASME B31.3 Pipe Code [35] is followed. Because of code restrictions, certain conventional approaches could not be implemented to calculate heat transfer coefficient.

Approach of obtaining local measurements by utilizing electrically heated foils over insulating substrate/wall, where paint-based or infrared measurements are used to indicate temperature distribution through optical access [36–38], cannot be used for current study. The setup must be rated for extreme pressure (200 bar). This can only be achieved using high grade materials such as stainless steel or Inconel.

Transient measurements with paints, over a thick insulating transparent substrate, where paint indicate change of temperature through some type of optical access [39–41] is also not feasible. Since the heating is done by providing electricity to the metal tubing,

the tubing cannot have any machining done. Otherwise this will cause non-uniformity in heat flux.

Approach of segmented heated copper-blocks with embedded thermocouples to give module-averaged heat transfer is usually used in internal duct cooling [42, 43]. Because of high pressure rating requirement, for this study the test section cannot be segmented. Segmentation causes flow to trip when passing a joint between two segments which can add unnecessary turbulence to the flow.

Considering all of the above restrictions, stainless steel is chosen as material for the loop and test section. Pressure de-rating of stainless steel is considered according to ASME B36.19M code [44]. This resulted in choice of 1/2″ stainless steel pipe with 0.065″ wall thickness which is rated at 350 bar at standard conditions. Outside surface temperature, inlet pressure, inlet and outlet bulk temperatures are utilized for data reduction process. Appropriate heat loss to ambient and axial conduction are also taken into account for heat balance while calculating heat transfer coefficient.

Description of experimental rig

For this paper, the experimental setup is in open loop configuration as shown in top of Figure 4.1. Inlet of the loop can be connected to a 100 psi air supply (for air validation cases) or sCO_2 supply from manifold of five CO_2 cylinders with maximum pressure of 10 MPa. The cylinders are used in a manifold assembly to increase the testing duration and providing a constant mass flow rate and pressure at the inlet. The inlet pressure is regulated by a pressure regulator before the inlet. The entire experimental loop is made of 1/2″ stainless steel pipe with 0.065″ wall thickness. All fittings for the loop are compression type fittings which makes the setup rated for 350 bar pressure at standard conditions. The stainless steel tube is surrounded by mineral wool insulation and encased

within PVC pipes to reduce heat loss to ambient. The experimental loop consists of an ON/OFF ball valve, instrumented test section, mass flow meter, a needle valve to control mass flow and two cord heaters.

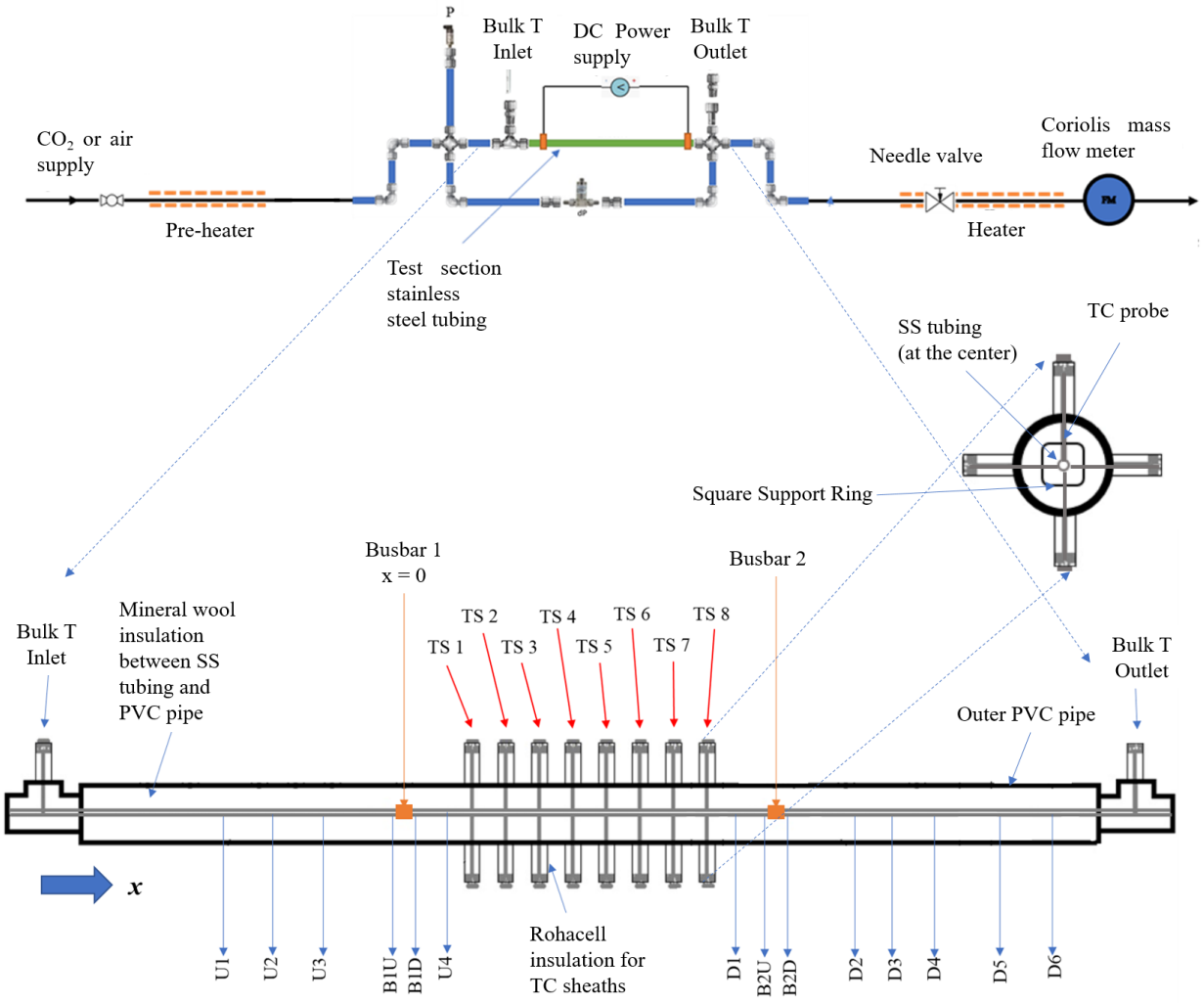

Figure 4.1: Schematic of experimental setup in open loop (top) and details of instrumented test section(bottom)

The first heater, named 'pre-heater' is used to control inlet bulk temperature of sCO_2. The heater downstream of the test section between needle valve and mass flow rate sensor is used to heat CO_2 coming out of needle valve. CO_2 experiences sudden drop in temperature due to sudden drop in pressure after passing through the needle valve. This phenomenon is called Joule-Thomson effect [45]. This Joule-Thomson effect causes a sudden drop in temperature of CO_2 which may lead to liquefaction or even formation of dry ice going into coils of Coriolis mass flow sensor. To prevent the damage to coils and erroneous mass flow rate reading due to liquefaction or formation of dry ice, temperature of CO_2 is raised using the rope heaters. Both heaters are 1000W fiberglass high temperature heating cords and are wrapped around stainless steel tube.

The experimental rig is located in the room which is equipped various safety measures. Continuously running positive ventilation system creates negative pressure in the room which can scoop out any leaked CO_2 and throw it into atmosphere. Very sensitive CO_2 sensors are scattered across the room at different heights and are able to alarm whenever CO_2 concentration increases above 1000 ppm. The exhaust of the loop is connected to a wind tunnel going outside into the atmosphere. This makes sure that all of CO_2 used for testing is released into atmosphere.

Description of test section

The detail of the test section with instrumentation is shown in bottom part of Figure 4.1. The test section is heated by passing electricity through stainless steel tubing. DC power supply is connected to the stainless steel test section using copper busbars, shown as Busbar 1 and Busbar 2 in Figure 4.1. The length between these two busbars is considered for heat transfer analysis. The DC power supply provides a uniform volumetric heat generation in heated length of the tube. The same DC power supply is used for moni-

toring and measuring of current. Concurrently, the voltage across the test section length is measured using a Keithley multimeter. A static pressure transmitter (measuring range of 0-250 bar) is used for monitoring and measuring inlet pressure. The test section consists of 8 thermocouple (TC) stations named from TS1 to TS8 located at 8 axial positions at distances 30d, 40d, ..., 90d, 100d starting from Busbar 1. At each TC station, outside wall temperatures is measured at 4 circumferential locations at 90°; top, right, bottom and left. Inlet & outlet bulk flow temperatures are measured by inserting TC probes into the flow. TCs used in 8 stations in the test section and for inlet and outlet bulk temperature are J-type TCs. Outside surface temperatures at upstream and downstream of the test section is measured by T-type TCs. The temperature distribution upstream and downstream is necessary for heat loss analysis, data reduction as well as heat balance. All the surface TCs used are un-grounded meaning the TC junctions do not touch the electrically heated metal surface directly. Using grounded TCs or exposed junction TCs can result in erroneous voltage output leading to erroneous temperature measurement.

Sources of systematic errors

Since the experimental setup is based on non-conventional approach for instrumentation, errors/losses occurring due to the same approach are also considered and accounted for while calculating heat transfer coefficient. Heat loss to ambient in radial direction is calculated by performing no-flow heated-tube tests. This radial heat loss also accounts for heat conducted through surface thermocouple probes. Copper busbars connecting stainless steel tube to wires of power supply can also conduct heat. That is why, busbars used here are in form of thin clamps instead of chunky plates to minimize heat loss. The stainless steel tube used here has considerable thickness of 0.065". This can result in axial conduction heat loss from heated section to unheated section. This axial

conduction and heat loss is considered in energy balance to calculate bulk temperature in the test section.

Heat loss tests

Since the setup requires accurate heat balance to calculate heat transfer coefficient, calculation of heat loss to the ambient through the insulation is vital. Hence heat loss tests are conducted with heated test section and no flow conditions. In addition to heat loss to ambient, axial conduction from heated section to unheated section is also important for heat balance. Figure 4.2 shows the thermal resistance model used for heat loss tests. Area specific overall heat transfer coefficient U_{ext} for heat loss in radial direction, based on pipe outer surface area is calculated for different heat flux cases. This overall heat transfer coefficient is the sum of individual resistances between outer surface of stainless steel tube and ambient as shown in Figure 4.2. The individual resistances such as conduction resistance due to mineral wool insulation, resistance due to PVC pipe and resistance due to natural convection in the room, are not calculated. The procedure directly calculates area specific overall heat transfer coefficient U_{ext}. These are presented in Table 4.1 for different power and ambient conditions. Mean of equivalent conductance is $U_{ext,mean}$ = 5.98 W/m^{2}K and the standard deviation is $\pm$ 0.23 W/m^{2}K which are used in data reduction and uncertainty analysis. Axial conduction from heated length to unheated length, especially upstream of Busbar 1 is also carried out for heat balance.

Data reduction

Area of cross section for the tubing is calculated using Equation 4.1.

$$A_{cs} = \pi \times [r_{ext}^2 - r_{int}^2] \tag{4.1}$$

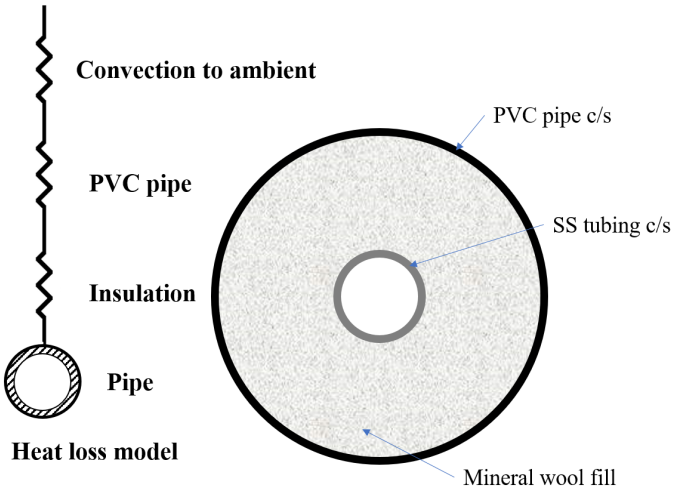

Figure 4.2: Pathway for radial heat loss to ambient

Table 4.1: Heat loss test summary: Equivalent heat loss coefficient calculated at the test section

Test	**Power [W]**	**T$_{amb}$ [^{o}C]**	**U$_{ext}$ [W/m^{2}K]**
1	7.42	25.5	5.84
2	21.42	28.6	6.25
3	10.21	25.7	5.68
4	13.21	26.3	5.98
5	13.37	29.3	6.13

Power provided to the test section is calculated using current provided by the DC power supply and voltage measured across the length (L_{total})of heated tubing excluding busbars' width.

$$Total\ measured\ power, POWER = V \times I \tag{4.2}$$

Heat transfer coefficient is calculated at four circumferential locations: top, bottom, left and right. Following data reduction is described for one 90^o quadrant with length L_{local}. This quadrant can be seen in Figure 4.3.

Local power is electric power generated in a local quadrant. Local length is the length of one quadrant where the heat transfer coefficient is calculated.

$$POWER_{local} = \frac{POWER \times L_{local}}{4L_{total}} \tag{4.3}$$

To calculate internal wall temperature, thermal conductivity of stainless steel and volumetric heat generation is required. Thermal conductivity of stainless steel being a function of temperature is calculated using Equation 4.5 [46]. Internal wall temperature is calculated using Equation 4.6.

$$q_{vl} = \frac{POWER}{L_{total}A_{cs}} \tag{4.4}$$

$$k_{SS} = 14.6 + 1.27 \times 10^{-2}T_{ext} \tag{4.5}$$

$$\begin{aligned} T_{w,int} = T_{w,ext} + q_{vl}/(4k_{SS})[r_{ext}^2 - r_{int}^2] \\ -q_{vl}/(2k_{SS})(r_{ext})^2 ln(r_{ext}/r_{int}) \end{aligned} \tag{4.6}$$

Heat loss to the ambient in radial direction is calculated using equivalent loss coefficient U_{ext} and temperature difference between external wall and ambient as shown in Equation 4.7. Area considered for this heat loss is outside surface area of a local quadrant.

$$Q_{loss,radial} = U_{ext}(T_w - T_{amb})L_{local}\frac{\pi D_{ext}}{4} \tag{4.7}$$

A large variation in temperature is observed within a cross-section. It is necessary to account for conduction heat transfer in circumferential direction due to the thick walled

stainless steel tubing. It is calculated using Equation 4.8. ΔT here is the temperature difference calculated between required circumferential locations including top, bottom, left and right.

$$Q_{cir,cond} = \frac{4 \times k_w \times \Delta T \times (r_{ext} - r_{int}) \times L_{local}}{(\pi \times (r_{ext} + r_{int}))} \tag{4.8}$$

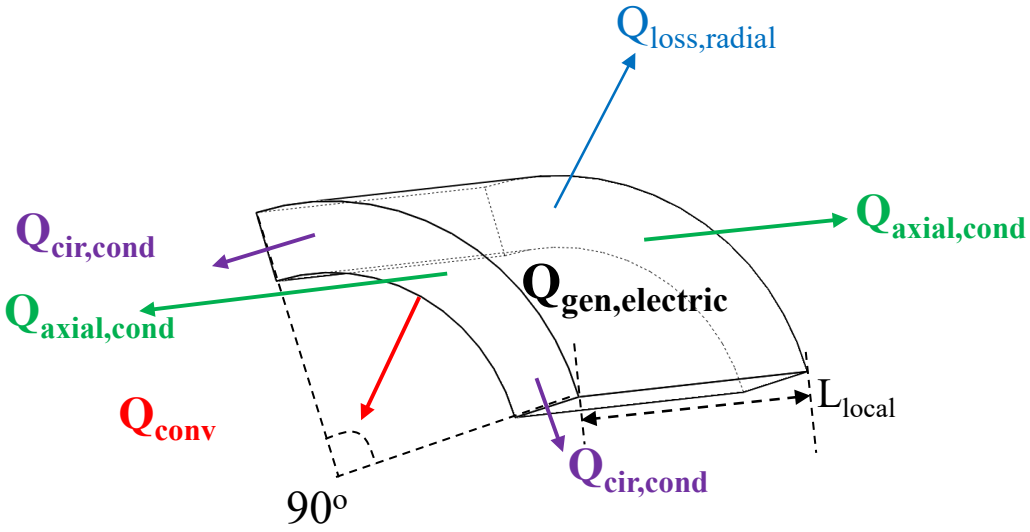

Figure 4.3: Heat balance in a quadrant

The energy balance to calculate heat transfer coefficient includes electric power, heat loss in radial direction and circumferential conduction as shown in Equation 4.9.

$$\Delta h_{local} = POWER_{local} - Q_{loss,radial} \pm Q_{cir,cond} \tag{4.9}$$

Enthalpy at each station is calculated from enthalpy at previous station and the heat transferred as shown in Equation 4.10.

$$h_x = h_{x-\Delta x} + \sum_{quadrant=1}^{4} \Delta h_{local} \tag{4.10}$$

Local bulk temperature is calculated using REFPROP with local enthalpy and pressure as inputs.

$$T_{bulk,x} = function(h_x, P) \tag{4.11}$$

Here, local pressure is assumed to be equal to inlet pressure. As explained earlier, it is difficult to measure local pressure since the stainless steel tube cannot have any machining done. However, estimated pressure drop is calculated by using friction factor correlations given by Filonenko [47] as well as Mikheev [48]. These friction factors are calculated according to Equations 4.12 and 4.13 as reported in [27]. Estimated pressure drop values are found to be within 10 Pa to 50 Pa. Such small difference in pressure do not affect values of thermodynamic properties to cause inaccuracies in heat transfer calculations. Hence for calculation of heat transfer coefficient, local pressure is assumed same as inlet pressure.

$$f_{Filonenko} = (1.82\, log_{10} Re_b - 1.64)^{-2} \tag{4.12}$$

$$f_{Mikheev} = (1.82\, log_{10} Re_b - 1.64)^{-2} \times \left(\frac{Pr_w}{Pr_b}\right)^{1/3} \tag{4.13}$$

Pressure drop is calculated using Equation 4.14 based on mass flux, G and local density ρ for local segments and added up to get outlet pressure.

$$\Delta P = \left(f \frac{G^2}{2\rho} \right) \tag{4.14}$$

Temperature difference between the bulk flow and the wall is used to calculate heat transfer coefficient as shown in Equation 4.15. One may argue validity of this equation in the presence of significant and potentially non-linear variation of fluid properties in the boundary layer. However, we have used the conventional definition.

$$HTC_{local} = \frac{\Delta h_{local}}{(T_{wall} - T_{bulk,x}) A_{local}} \tag{4.15}$$

Local CO_2 thermal conductivity for bulk flow is calculated using REFPROP [49] with local enthalpy and pressure as inputs. This value of CO_2 thermal conductivity is used in calculation of local Nusselt number as shown in Equation 4.17.

$$k_{CO_2,bulk,x} = function(h_x, P) \tag{4.16}$$

$$Nu_{local} = \frac{HTC_{local} D_{int}}{k_{CO2,bulk,local}} \tag{4.17}$$

Nusselt number is calculated from Gnielinski correlation [50] and Dittus-Boelter correlation using bulk property values as follows.

$$Nu_{Gn} = \frac{(f/8)(Re_b - 1000) Pr_b}{1 + 12.7(f/8)^{0.5}(Pr_b^{2/3} - 1)} \tag{4.18}$$

$$Nu_{DB} = 0.023 Re_b^{0.8} Pr_b^{0.4} \tag{4.19}$$

Uncertainty analysis

The uncertainty analysis is based on methods described by Kline and McClintock, [51], Moffat [52] and the Test Uncertainy Standard PTC 19.1 - 2005 by the American Society of Mechanical Engineers (ASME) [53]. Measurement uncertainties for all instruments used are listed in Table 4.2. Uncertainties in thermodynamic properties derived from REFPROP are neglected as suggested by a report by National Institute of Standards and Technology (NIST) [54]. Error propagation in heat transfer coefficient is calculated using Equations 4.21, 4.22, 4.23 and 4.24.

$$\left(\frac{\delta_{POWER_{local}}}{POWER_{local}}\right) = \pm 1.63\% \tag{4.20}$$

$$\begin{aligned} {\delta_{T_{w,int}}}^2 = \\ \delta_{T_{w,ext}}^2 + \left(\delta_{POWER_{local}} \left[\frac{r_{ext}^2 - r_{int}^2 - 2(r_{ext})^2 ln(r_{ext}/r_{int})}{4k_{SS}}\right]\right)^2 \end{aligned} \tag{4.21}$$

$$\frac{\delta_{Q_{loss,radial}}}{Q_{loss,radial}} = \sqrt{\left(\frac{\delta_{U_{ext}}}{U_{ext}}\right)^2 + \left(\frac{\delta_{T_w}}{T_w}\right)^2 + \left(\frac{\delta_{T_{amb}}}{T_{amb}}\right)^2} \tag{4.22}$$

$$\frac{\delta_{Q_{cir,cond}}}{Q_{cir,cond}} = \frac{\delta_{T_w}}{T_w} \tag{4.23}$$

$$\begin{aligned} {\frac{\delta_{HTC}}{HTC}}^2 = \left(\frac{\delta_{POWER_{local}}}{POWER_{local}}\right)^2 + \left(\frac{\delta_{Q_{loss}}}{Q_{loss}}\right)^2 + \left(\frac{\delta_{Q_{cir,cond}}}{Q_{cir,cond}}\right)^2 \\ + \left(\frac{\delta_{T_{wall}}}{T_{wall}}\right)^2 \end{aligned} \tag{4.24}$$

Table 4.2: Uncertainties of measured parameters

Parameter	**Uncertainty**
Test section power	$\pm$ 1.63%
Inlet pressure	$\pm$1.9%
Temperatures	2.2^o C
Mass flow rate	$\pm$0.98 %

Table 4.3: Nusselt number uncertainty summary

Maximum uncertainty	9.70%
Minimum uncertainty	4%
Average uncertainty	6.80%

Uncertainty in heat transfer coefficient is same as uncertainty in Nusselt number given negligible uncertainty in thermal conductivity of the tube. Table 4.3 shows summary of uncertainty calculated for Nusselt numbers. The source of highest error was found to be the temperature measurements.

Validation with high pressure air heat transfer experiments

Validation experiments with high pressure air were conducted as a means to establish the baseline confidence interval for the sCO_2 tests. Experiments with same testing conditions are carried out on different days to check repeatability. For air experiments, inlet was connected to high pressure air supply from a compressor.

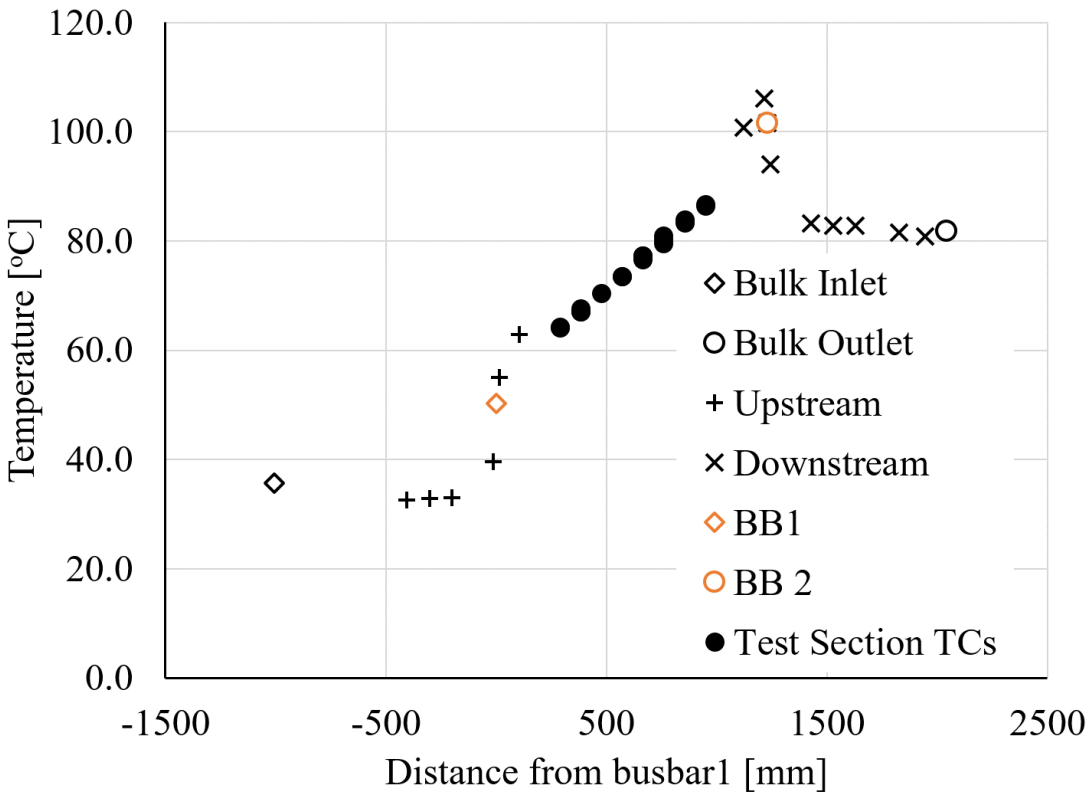

Figure 4.4: Measured temperatures for air validation case 7 (as mentioned in Table 4.4)

Maximum testing pressure at inlet was ≈ 6.9 bar (100 psi) with maximum surface temperature observed around ≈ 370K. The compressor could provide a steady mass flow rate for more than two hours which was sufficient time to reach the steady state data. Raw wall temperatures, bulk flow inlet and outlet temperatures, upstream and downstream wall temperatures can be seen in Figure 4.4. x=0 is defined at the busbar 1. For air heat transfer cases, circumferential variation in temperature is negligible. Temperature gradient between the heated and unheated potion of tubing can create considerable axial conduction. As mentioned before, this conduction is taken into account for heat balance in data reduction. There is uniform thermal gradient within the test section (solid

black circles in Figure 4.4), indicating negligible axial conduction in the heated test section. Because the incoming axial conduction from downstream is equal to outgoing axial conduction to upstream. Within the test section, measured wall temperatures and calculated bulk temperatures (Figure 4.5) are used to calculate heat transfer coefficient and Nusselt number.

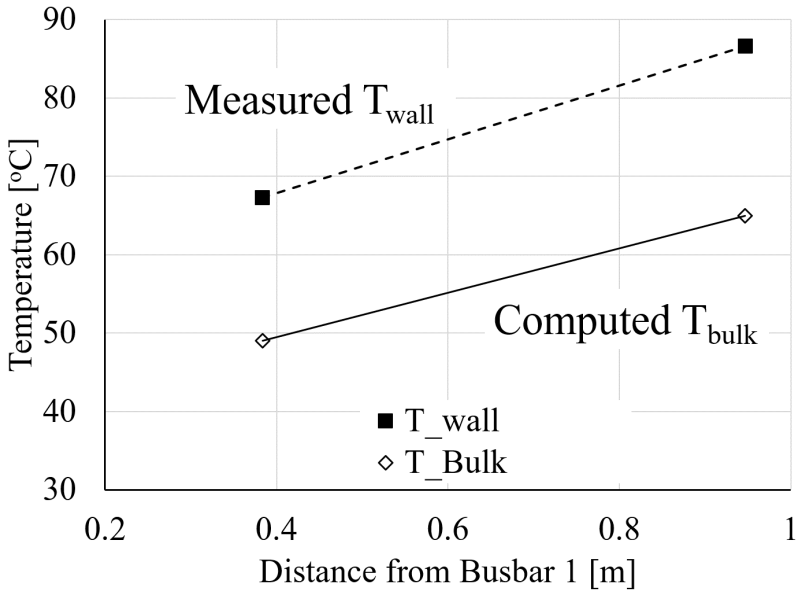

Figure 4.5: Wall temperature vs Bulk flow temparture comparison for air validation case 7 (as mentioned in Table 4.4)

Summary of air heat transfer experiments is shown in Table 4.4. Nusselt number calculated using experiments are within $\pm$ 9% of Nusselt number obtained using conventional correlations.

Table 4.4: Air validation experiments summary. Dittus-Boelter (DB), Gnielinski (Gn)

Case	**Re**	**Heat flux**	**P_{in}**	**Nu**	**Nu**	**Nu**
	[-]	**[kW/m^2]**	**[bar]**	**expt**	**DB**	**Gn**
1	21210	3.69	6.69	57.2	56.3	52.7
2	21694	3.76	6.76	56.2	57.3	53.7
3	21739	3.73	6.76	54.5	57.5	53.8
4	21814	3.77	6.77	54.5	57.6	53.9
5	21872	3.81	6.7	58.7	57.7	54.0
6	17491	2.88	7.2	48.7	48.4	45.5
7	12,700	2.45	3.4	38.1	37.6	35.5

	Dittus-Boelter	**Gnielinski**
Maximum deviation	2%	9%
Minimum deviation	-5%	1%
Average deviation	-1%	6%

CHAPTER 5: RESULTS AND DISCUSSION

Newton's law of cooling for internal flows

Convection heat transfer within a fluid can be described as energy transfer due to diffusion (also known as 'conduction') and bulk fluid motion (also known as 'advection'). Newton's law of cooling is considered as basis of convection heat transfer. In his original paper [55] which is in Latin language, Newton suggested that the rate at which a hot body cools down should be proportional to temperature difference between the hot body and its surrounding. Although his study was meant for establishing new temperature scale and measuring high temperatures, it received more attention to define convective heat transfer equation.

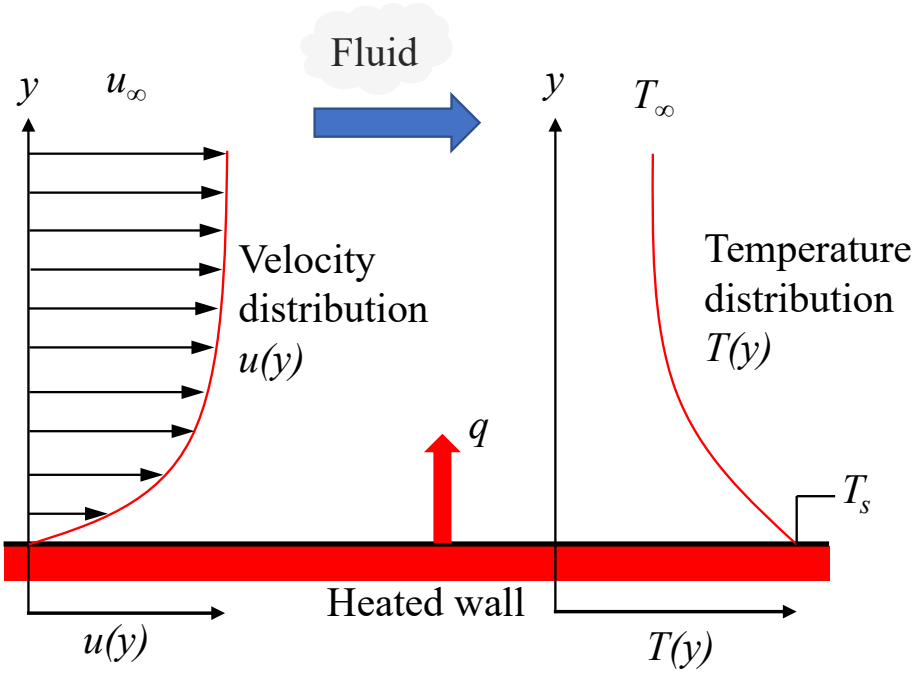

Figure 5.1: Boundary layer development on heated wall surface

Contemporary form of Newton's law of cooling found in most of the textbooks is as follows:

$$Q = hA(T_s - T_\infty), \tag{5.1}$$

where Q is heat flow rate, h the heat transfer coefficient, A the surface area, T_s the temperature of the solid surface and T_∞ the temperature of the coolant fluid. Figure 5.1 shows hydrodynamic boundary layer where the velocity varies from zero at the wall to free stream velocity, u_∞. At the same time, wall and surrounding fluid are at different temperature causing formation of thermal boundary layer in which temperature varies from T_s at wall to T_∞. This is the most popular form of defining convective heat transfer coefficient.

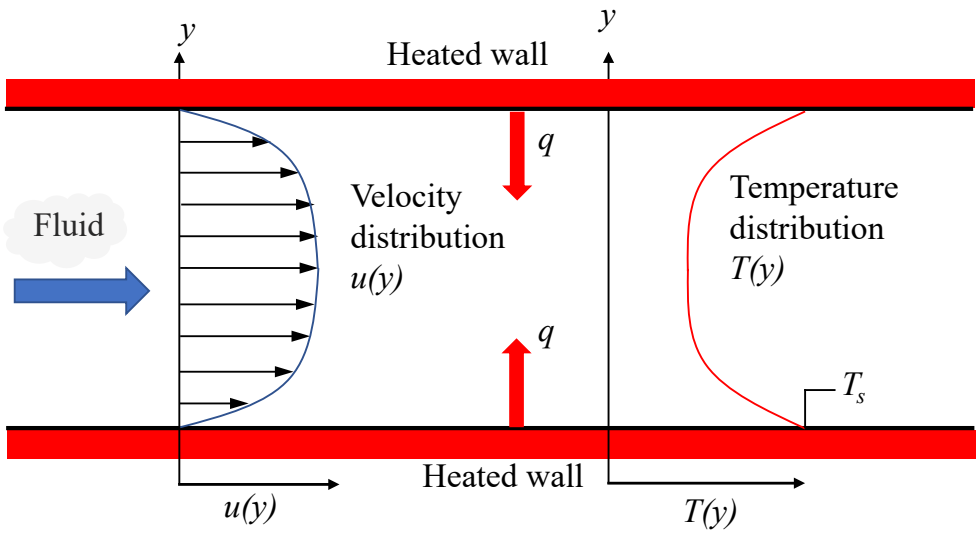

Figure 5.2: Boundary layer development on heated wall surface for internal flow

For internal flows, boundary layer from walls at all directions merge at the centerline after certain length in flow direction: this length is called entrance length or the

region of flow development. Region after the entrance length is called as fully developed flow region. Since concept of 'free-stream' cannot be defined for internal flows, bulk temperature is used to calculate heat transfer coefficient. This bulk, or sometimes also called mean temperature is defined as follows:

$$mc_pT_{bulk} = \int_{A_c} \rho u c_p T dA_c \tag{5.2}$$

$$T_{bulk} = \frac{\int_{A_c} \rho u c_p T dA_c}{mc_p} \tag{5.3}$$

Based on bulk temperature, for heated wall case, Newton's law of cooling can be expressed as,

$$q = h(T_s - T_{bulk}) \tag{5.4}$$

Equation 5.4 has been heavily used in literature to calculate heat transfer for internal flows in pipes and to develop empirical correlations for heat transfer coefficient and Nusselt number. It has also been used to develop Nusselt number correlations for sCO_2 flows in vertical direction. ***However, a question can be raised whether it can be used to calculate heat transfer coefficient in supercritical CO_2 horizontal flows where flow properties undergo drastic variations between wall and centerline.***

For flow inside a tube, temperature profile as a function of distance from wall can be calculated using thermal law of the wall Equation 5.5 which is a relation between T^+ and y^+ as given in [56]. It is important to note that equation 5.5 is valid neither inside viscous sublayer nor at the tube centerline.

$$T^+ = 2.2\, lny^+ + 13.39\, Pr - 5.66 \tag{5.5}$$

Profiles of temperature and other thermophysical properties such as density, specific heat capacity, thermal conductivity and Prandtl number can be seen in Figure 5.3. Here y represents height from the internal wall and y/r = 0 represents internal wall of the tube. All the properties shown in Figure 5.3 are plotted as their ratio to corresponding property value at the wall as listed in Table 5.1. This means at y/r = 0, ratio for all of these property is equal to 1. Case shown for air is from air validation case 7 as shown in Table 4.4 and case shown for CO_2 is from case HF4 as shown in Table 5.3.

As seen from Figure 5.3, variations for air case are smaller than variations for CO_2 case. Specifically for specific heat and Prandtl number, for case of CO_2, the variation from wall property is $\approx$ 1.25-1.3 whereas for air it is $\approx$ 1. For CO_2 case, density also varies a lot compared to air case. Specific heat capacity is used to calculate bulk temperature (Equation 5.3) which itself is used to calculate heat transfer coefficient. For case of CO_2, specific heat can vary a lot within a cross section as shown in Figure 5.3. This raises a question whether conventional approach to calculate heat transfer coefficient using bulk temperature definition applies for sCO_2 heat transfer cases.

One may argue validity of Equation 5.1 in the presence of significant and potentially non-linear variation of fluid properties in the boundary layer. However, here the conventional definition of heat transfer coefficient is used.

Table 5.1: Values of properties at wall for plots shown in Figure 5.3

	Property value at wall				
	T	**Density**	**Cp**	**Pr**	**k**
	[K]	*[kg/m^3]*	*[J/kg.K]*	*[-]*	*[W/m.K]*
Air case	357	3.5	1012	0.70	0.031
CO_2 case	400	113.7	1200	0.87	0.029

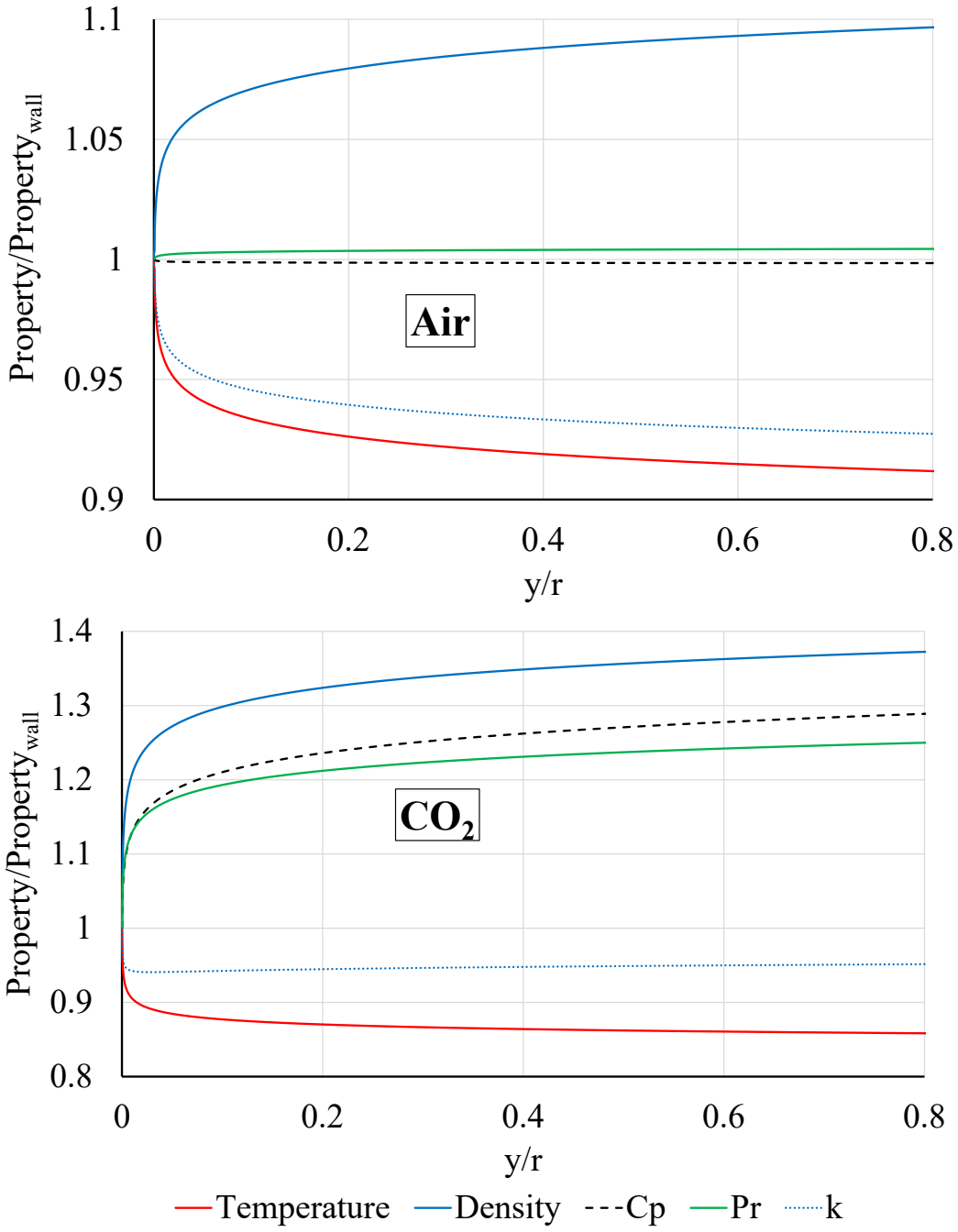

Figure 5.3: Profile of properties as ratio to properties at wall according to thermal law of the wall: Top- air validation case 7 as shown in Table 4.4, Bottom- case HF4 as shown in Table 5.3

Open loop supercritical CO_2 heat transfer

Open loop sCO_2 experiments are performed near critical region with three varying conditions: heat flux, inlet temperature and mass flux. For each set of experiment, for one variable condition, other two conditions are kept constant. Details of inlet conditions of these experiments are shown in Table 5.3, Table 5.2 and Table 5.4 respectively. To estimate and quantify buoyancy effects on heat transfer, parameters based on Reynolds number, Grashof number and Prandlt number are used here [23]. Grashof number and Richardson number is calculated as shown in Equation 5.6 and 5.7, respectively. Jackson [23] presented a modified form of Grashof number based on wall and bulk density, Bu_j as shown in Equation 5.8. It has been reported [24, 57–60] that buoyancy is negligible when Ri is less than $1/1000$ or when Bu_j is less than 10.

$$Grashof\ number,\ Gr = \frac{(\rho_w - \rho_b)\ \rho_b\ g\ d^3}{\mu_b^2} \tag{5.6}$$

$$Ri = \frac{Gr}{Re_b^2} \tag{5.7}$$

$$Bu_j = \frac{Gr}{Re_b^2}\frac{x^2}{D^2}\frac{\rho_b}{\rho_w} \tag{5.8}$$

It has been reported that pseudocritical temperature plays important role in sCO_2 heat transfer. Pseudocritical temperature at a specified pressure is defined in Equation 5.9 [61].

$$\begin{aligned} Tpsc = -122.6 + 6.124P - 0.1657P^2 + 0.01773P^{2.5} \\ -0.0005608P^3 \end{aligned} \tag{5.9}$$

where Tpsc is in ^{o}C and P is in bars. Ratio of bulk flow temperature to pseudocritical temperature, T_{bulk}/T_{psc} is plotted for all cases to discuss its effect on heat transfer.

Circumferential variation in heat transfer

For case HF4 as shown in Table 5.3, circumferential variation in temperature, density and Nusselt number is plotted in Figures 5.4, 5.5 and 5.6, respectively. Figure 5.4 shows difference between temperature at inside wall locations and temperature calculated for bulk fluid. It is important to note that bulk fluid temperature does not necessarily mean centerline temperature.

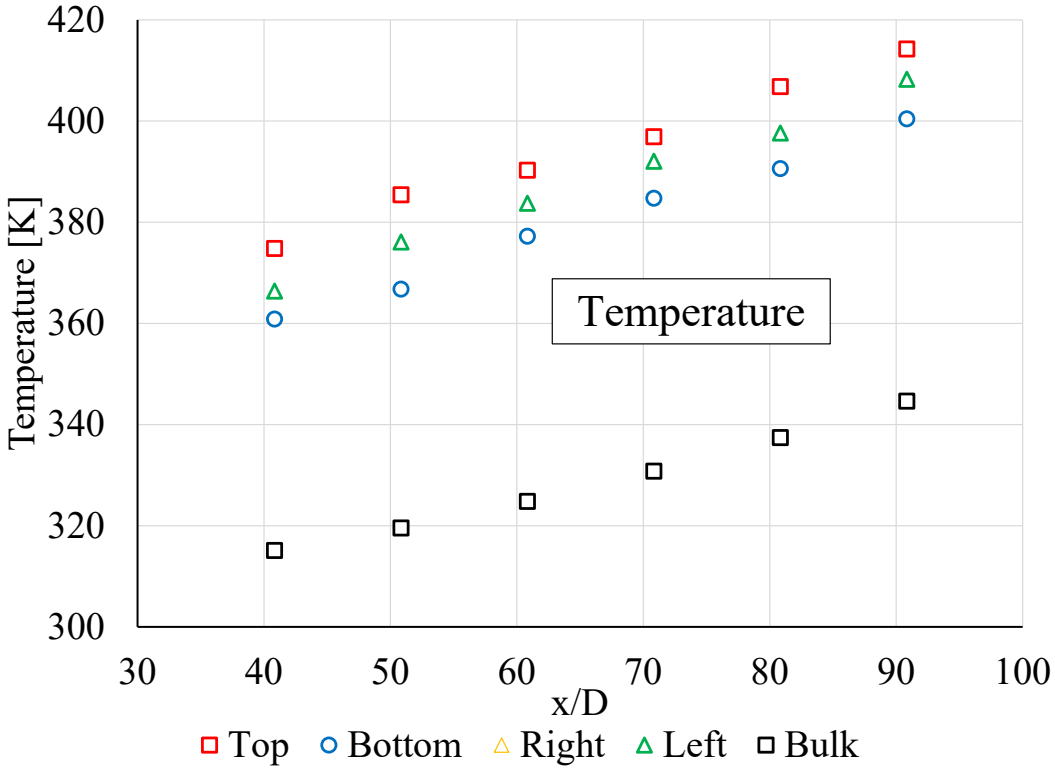

Figure 5.4: Circumferential variation in temperature plotted for case HF4 as listed in Table 5.3

Figure 5.5: Circumferential variation in density plotted for case HF4 as listed in Table 5.3

Temperature at centerline may even be less than the bulk fluid temperature. This difference in temperature between wall and bulk causes difference in density also. Density at walls is lower density than calculated density at bulk as shown in Figure 5.5. This causes natural convection from bottom wall to top wall as illustrated in Figure 5.7.

As a result of this buoyancy due to density gradient in a cross-section, heat transfer at the bottom wall is increased and is higher than the top wall. This can be seen in Figure 5.6, with highest Nusselt number for bottom wall and lowest for top wall. Nusselt number plotted using Dittus-Boelter and Gnielinski correlations use bulk properties such as Prandtl number, density and viscosity. It can be seen that experimentally calculated Nusselt number in the cross section does not follow Nusselt number based on conven-

tional correlations. ***For the two cases plotted in Figure 5.6, it can be seen that it is not always necessary that Nusselt numbers calculated from Dittus-Boelter and Gnielinski correlations will equal to Nusselt number a specific wall locations.***

It is interesting to note that temperature, density and Nusselt number are identical for right wall and left wall. All the measured and calculated values for right wall and left wall are between bottom wall and top wall values. Hence, for further analysis all the results corresponding to right and left wall is shown only as results for side wall. There was no fixed trend of Nusselt number in the axial direction. This is also reported by Kim et. al. [22] for cases with low heat flux. This leads author to believe the flow may not be fully developed. Henceforth, in this study, main emphasis is given on heat transfer trends at top, bottom and side wall surfaces due to effects of different testing conditions.

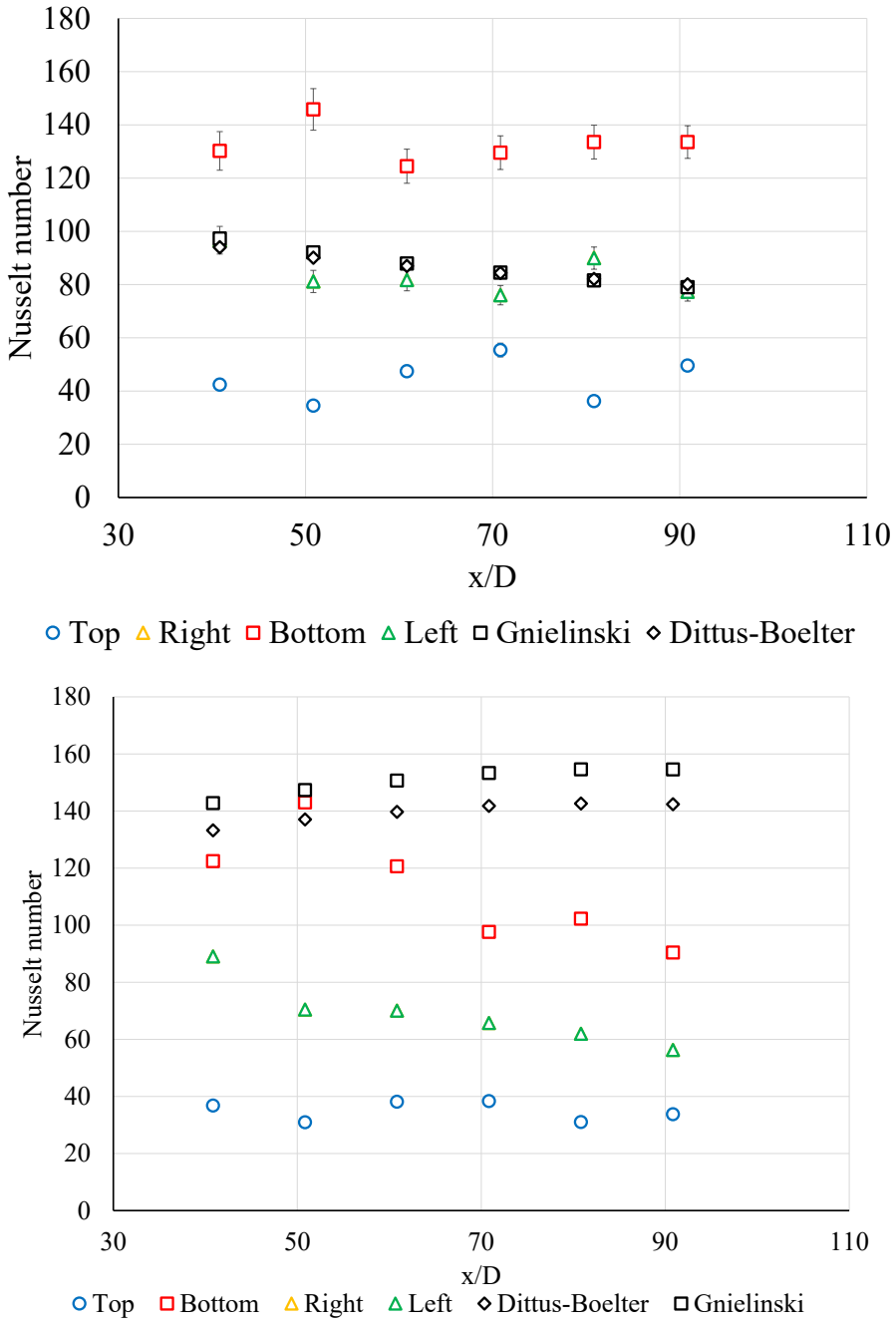

Figure 5.6: Circumferential variation in Nusselt number for two different cases. For top plot- 74.4 bar, 54 kg/m^{2}s, 11.8 kW/m^2, Re$_{inlet}$ = 21,400. For bottom plot- 88.7 bar, 76 kg/m^{2}s, 6.8 kW/m^2, Re$_{inlet}$ = 16,650

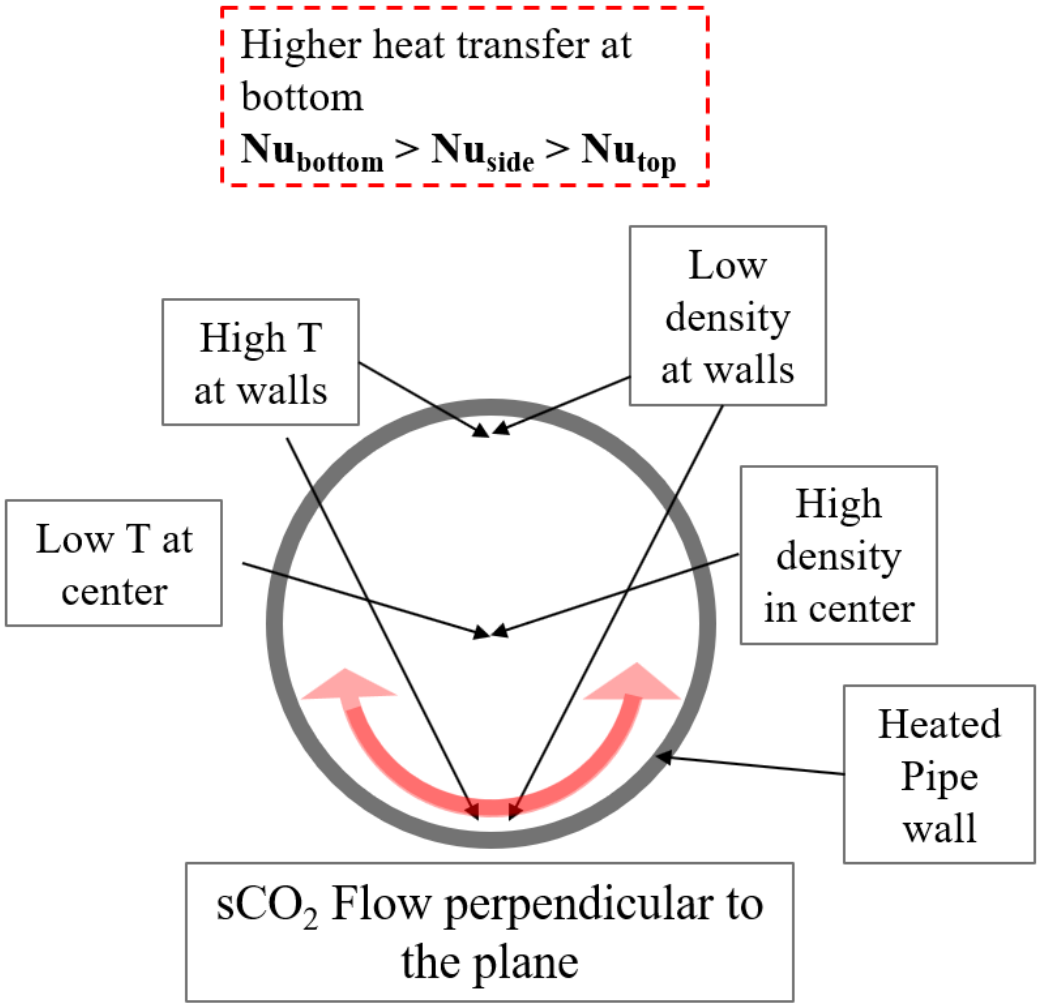

Figure 5.7: Schematic of cross section of tube showing natural convection current from bottom wall to top wall (CO_2 flow direction going into the page)

Effects of mass flux variation

Operating conditions for varying mass flux tests are shown in Table 5.2. Figure 5.8 shows results for varying mass flux cases with constant heat flux of 4.9 kW/m^2. Lowest mass flux cases has highest Nusselt number at the bottom wall and lowest Nusselt number at the top wall. In other words, highest heat transfer enhancement at bottom and highest heat transfer deterioration at the top wall for lowest mass flux cases. This enhancement of heat transfer at the bottom wall reduces with increasing mass flux. This means that effects of buoyancy increases with reduced mass flux. This is also evident from definition of Grashof number which is inversely proportional to square of Reynolds number. Nusselt number at the side wall were observed to be within the values at bottom wall and top wall for all cases.

Table 5.2: Testing conditions for varying mass flux cases with constant heat flux of 4.9 kW/m^2

Case	**T**$_{bulk,in}$	**P**$_{in}$	**Mass flux**	**Re**$_{in}$
	[^{o}C]	**[bar]**	**[kg/m^{2}s]**	
MF1	34.68	74.19	50	21703
MF2	34.7	74.07	70	30502
MF3	34.5	74.45	80	34536

This is also reflected in the values of Richardson number (Ri) and Jackson buoyancy parameter, (Bu$_j$). Figure 5.10 and 5.9 show effects of mass flux on buoyancy parameters on bottom wall and top wall, respectively. The buoyancy parameters decrease with increasing value of mass flux since Grashof number is included in their definition. Bu$_j$ is observed to increase along length of the tube while Ri is observed to decrease along length of the tube. This is mainly because of the dominant (x/D)^2 term in expression for Bu$_j$. Hence Ri indicates that buoyancy effects get weaker downstream and Bu$_j$ indicates that buoyancy effects get stronger downstream.

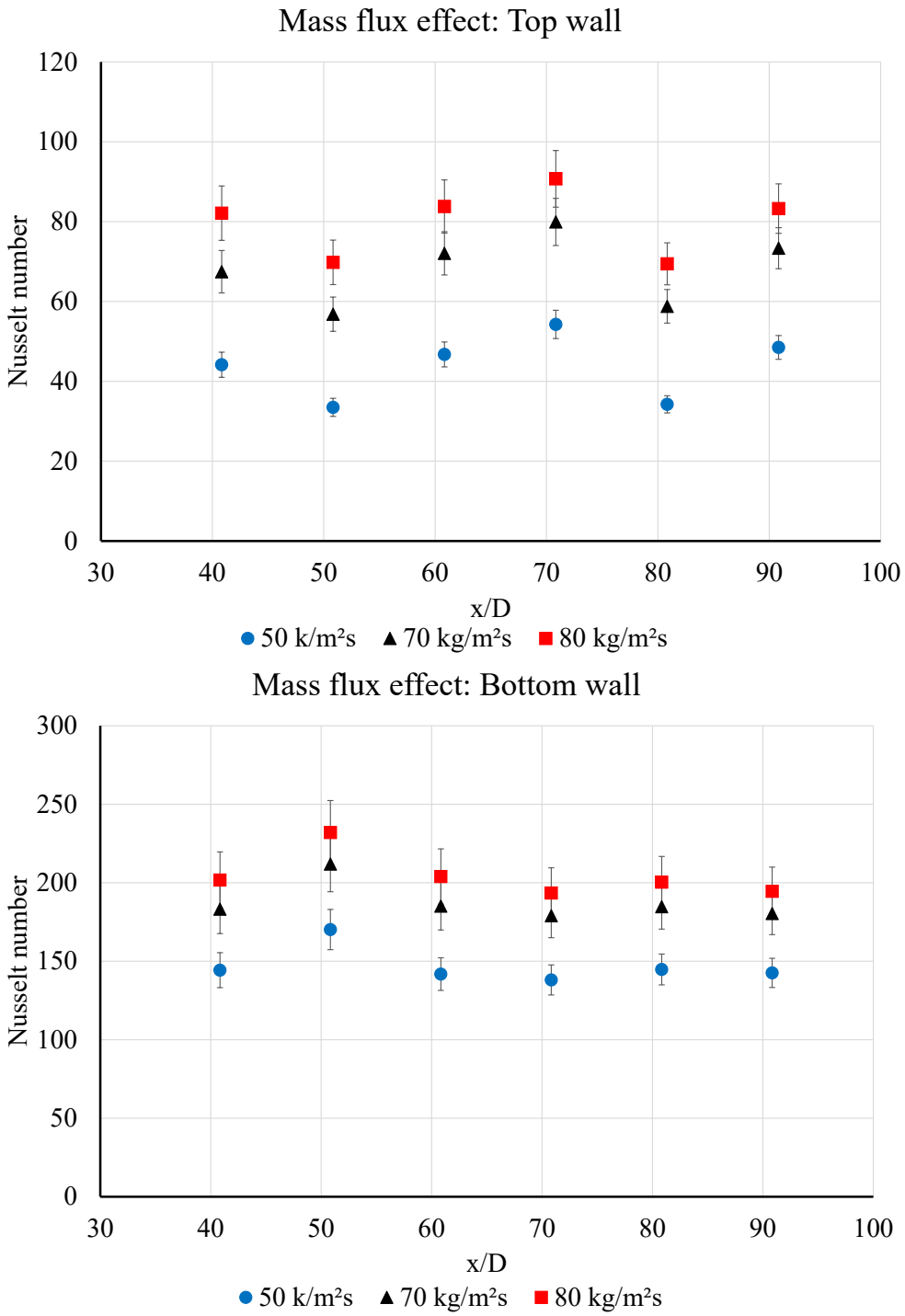

Figure 5.8: Variation of Nusselt number with mass flux

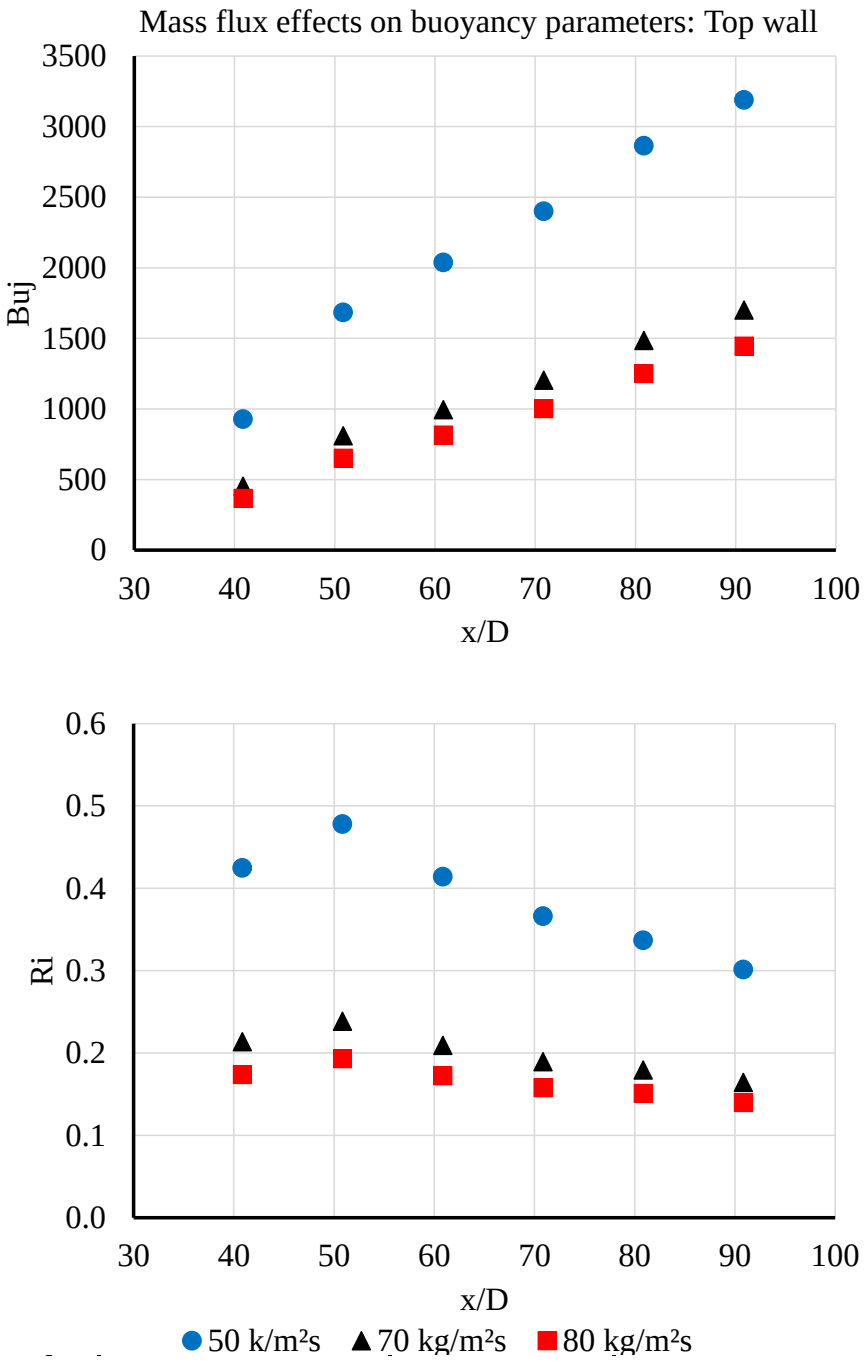

Figure 5.9: Variation in buoyancy parameters with mass flux at top wall

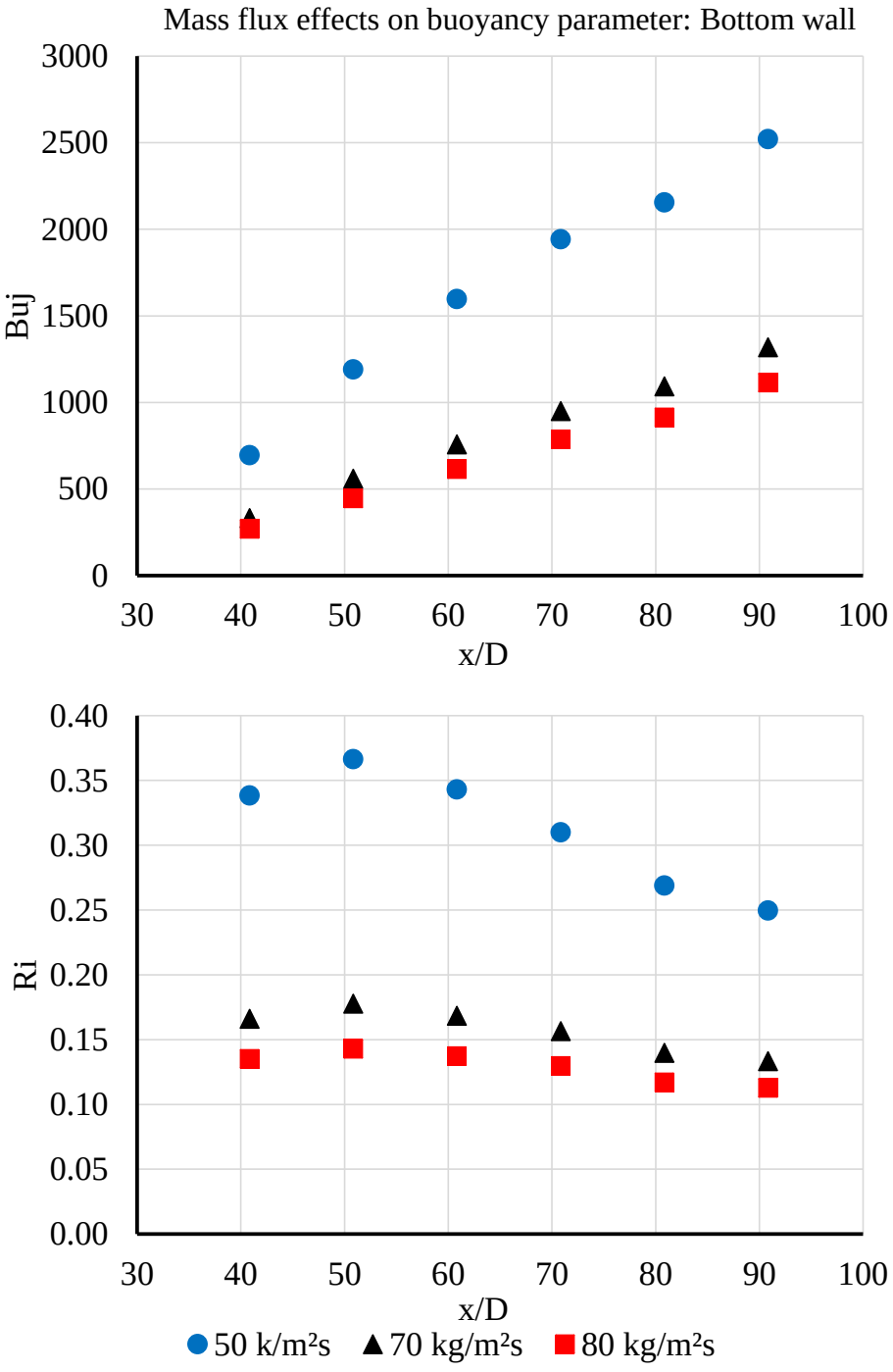

Figure 5.10: Variation in buoyancy parameters with mass flux at bottom wall

Effects of heat flux variation

Table 5.3 lists operating conditions for tests with varying heat flux. For these tests, mass flux and inlet temperature are kept constant. With increasing heat flux, it is expected that effects of buoyancy due to natural convection becomes dominant whereas forced convection remains comparable. For the cases studied here, increasing heat flux resulted in increase of Nusselt number at all the wall locations. This can be seen in Figure 5.11. To study the effects of heat flux on buoyancy, Figure 5.12 shows difference between Nusselt number at bottom and top locations. With increase in heat flux, this difference also increases. This proves that increasing heat flux increases the effects of buoyancy on sCO_2 heat transfer.

Table 5.3: Testing conditions for varying heat flux cases with constant mass flux of 54 kg/m^2s

Case	$\mathbf{T}_{bulk,in}$	$\mathbf{P}_{in}$	**Heat flux**
	[^{o}C]	**[bar]**	**[kW/m^2]**
HF1	32.6	74.8	2.7
HF2	32.2	74.3	4.9
HF3	32.6	74.2	7.9
HF4	32.5	74.4	11.8

However, this is not reflected in trends of buoyancy parameters. Both Ri and Bu_j reduce with increasing heat flux at all wall locations. This is mainly because both of these parameters do not consider the effects of varying heat flux. Similar results were also shown by Tanimizu & Sadr [33] and Kim et. al. [22] in their work on investigating validity of these buoyancy parameters.

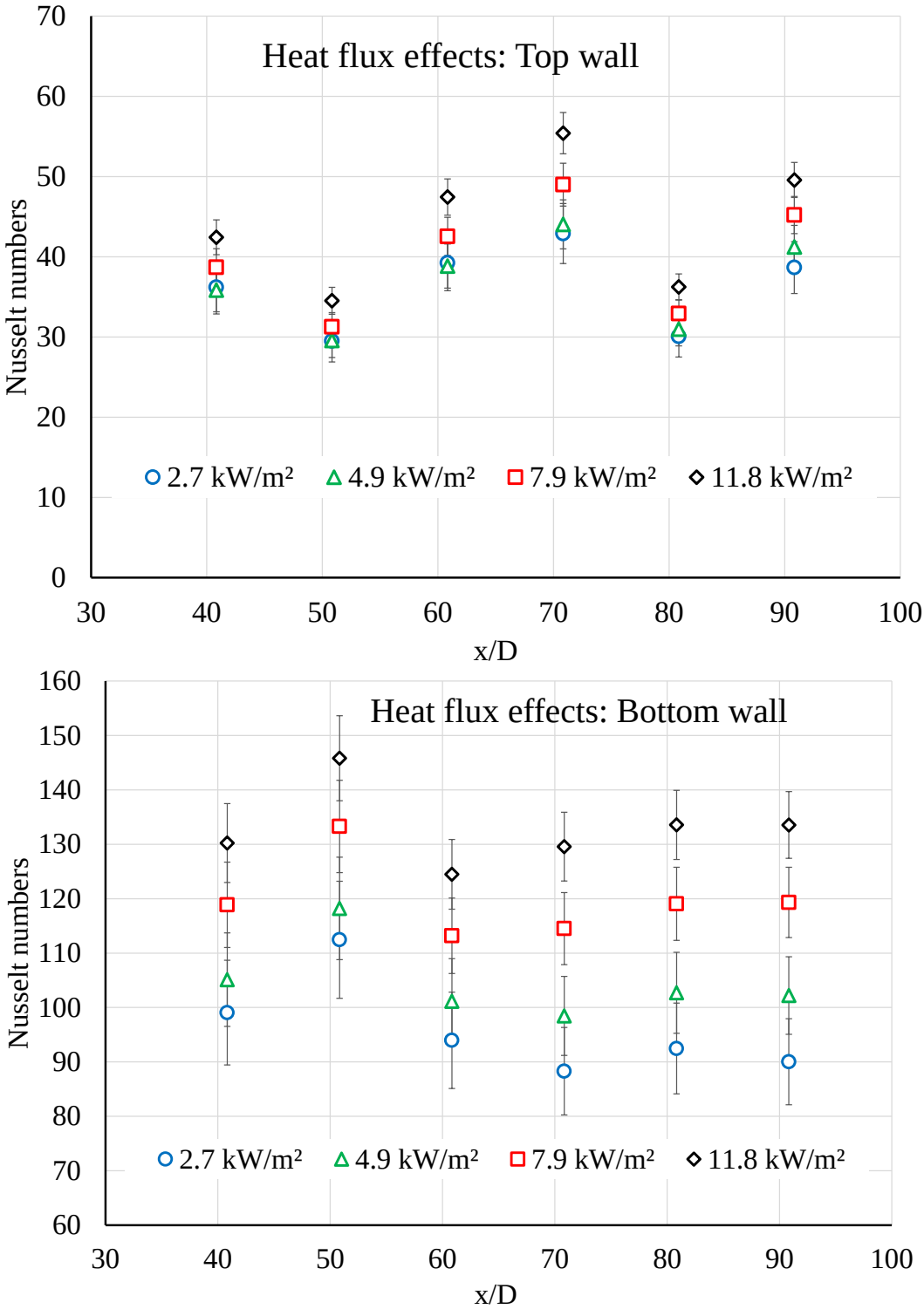

Figure 5.11: Variation of Nusselt number with heat flux

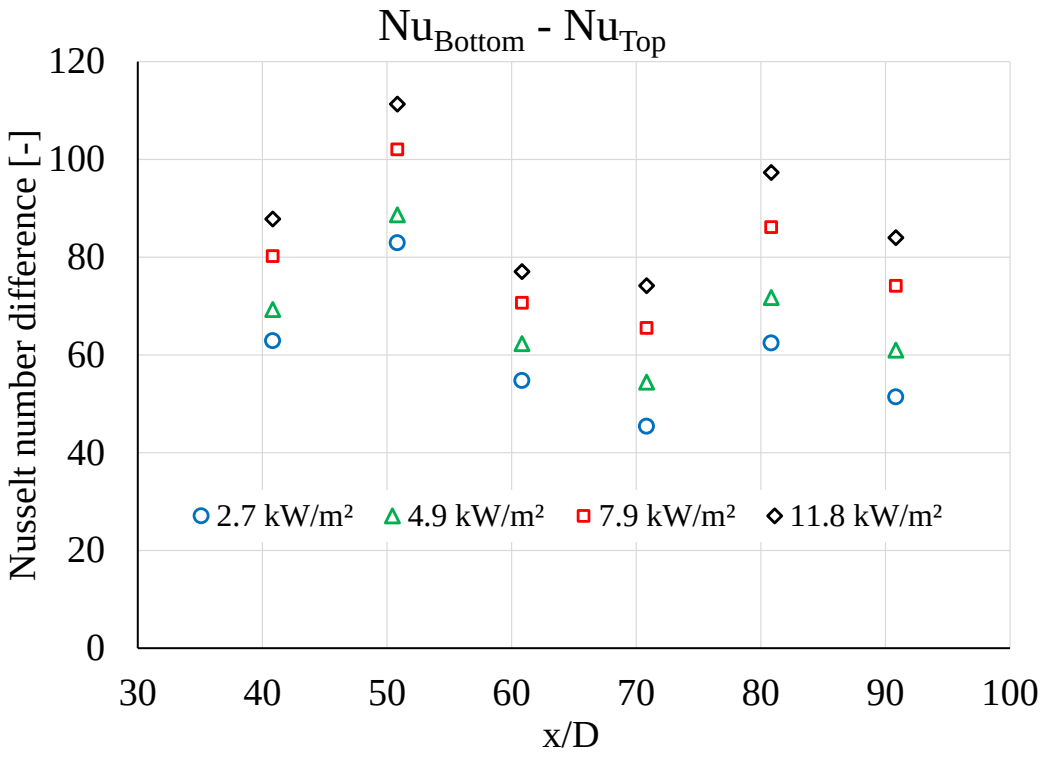

Figure 5.12: Difference in Nusselt number at bottom and at top wall location with heat fluxes

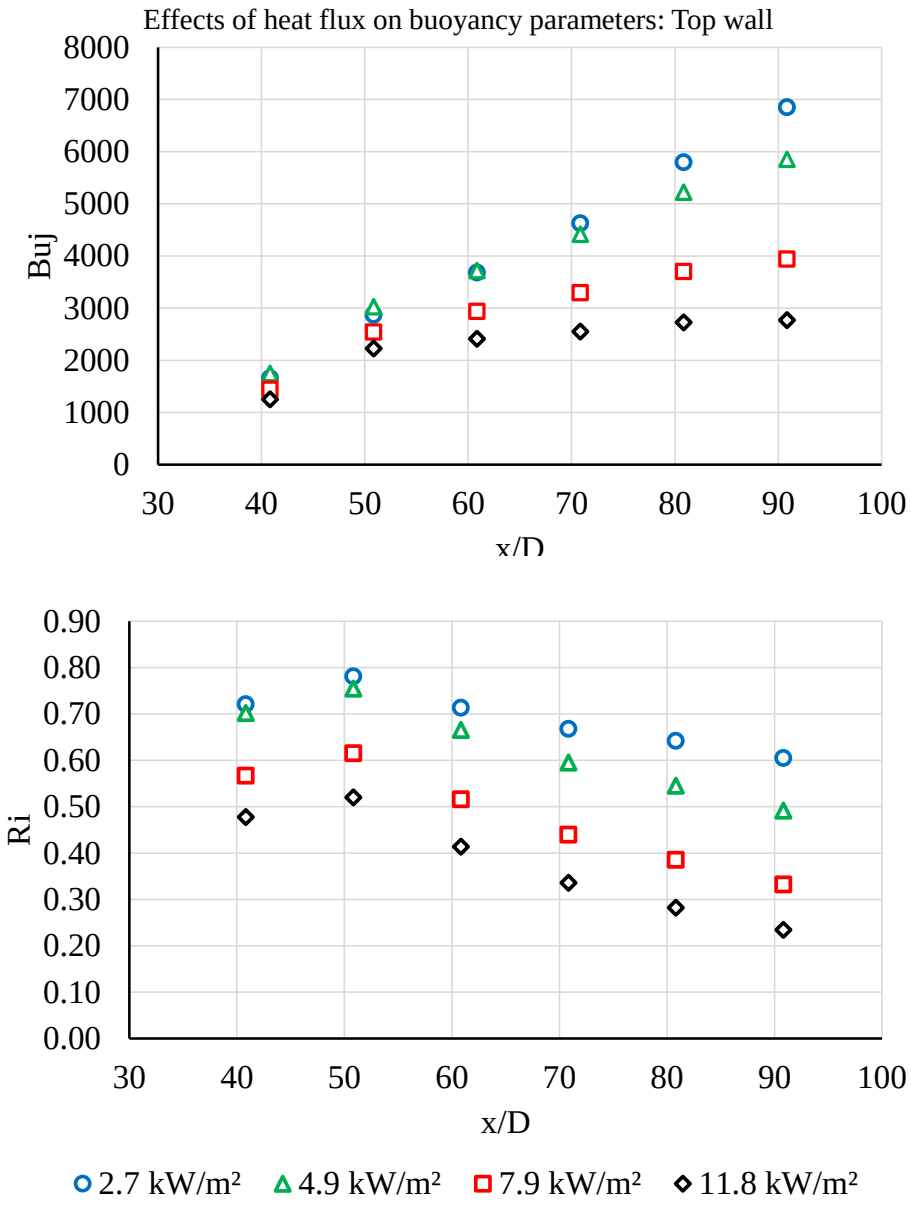

Figure 5.13: Variation in buoyancy parameters with heat flux at top wall

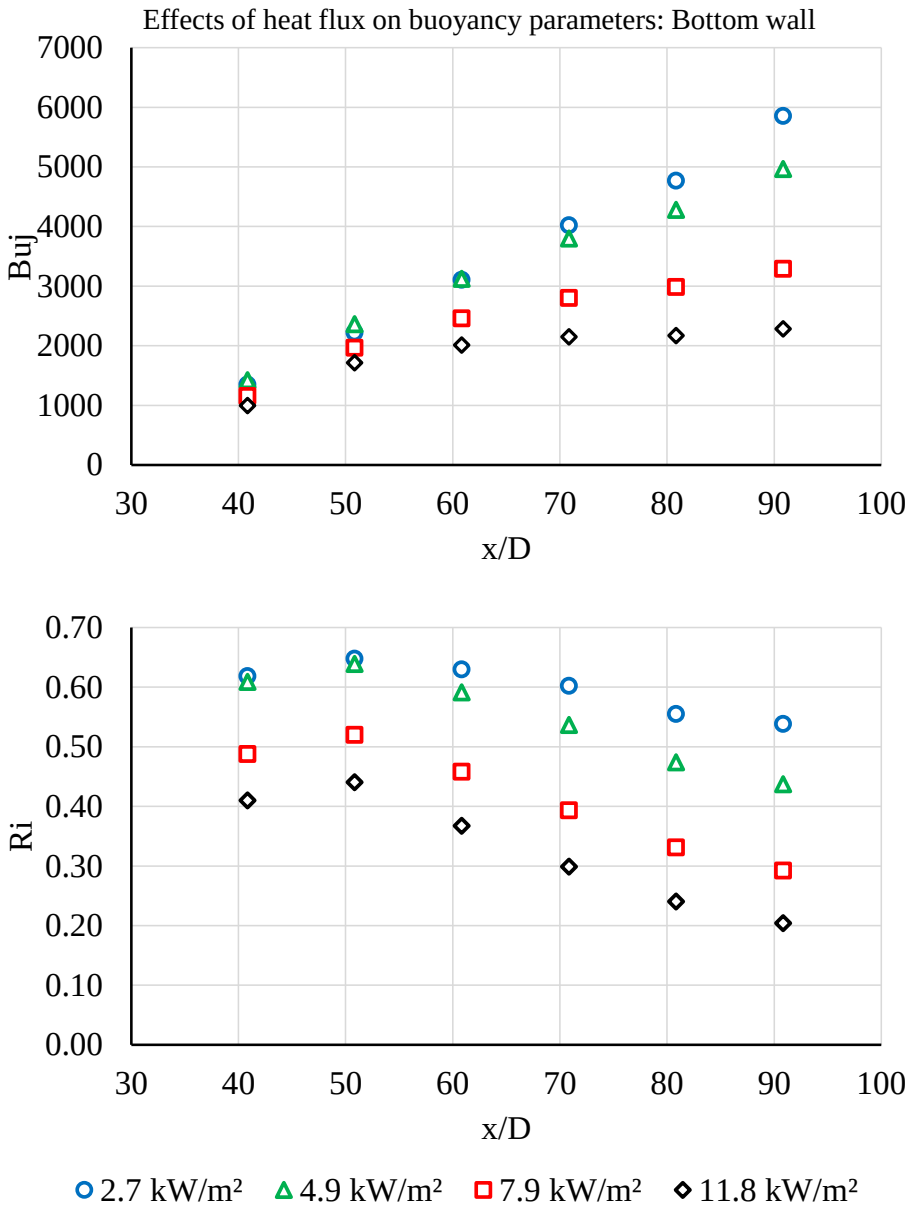

Figure 5.14: Variation in buoyancy parameters with heat flux at bottom wall

Effects of inlet temperature variation

Previous cases with varying mass flux and heat flux are performed close to critical pressure and at temperatures closer to but slightly higher than pseudocritical temperature. To investigate effects of buoyancy away from pseudocritical region, five different tests as listed in Table 5.4 are performed with increasing inlet temperature. Effects of increasing temperature is best seen in variation of difference between wall temperature and bulk temperature (Figure 5.15) and variation of density difference between wall locations and bulk (Figure 5.16). For both of these parameters, as temperature moves away from pseudocritical temperature, the difference decreases. This indicates effects of buoyancy decrease away from pseudocritical temperature.

Table 5.4: Testing conditions for varying inlet temperature cases with constant mass flux of 50 kg/m^{2}s and constant heat flux of 4.9 kW/m^2

Case	**T**$_{bulk,in}$	**P**$_{in}$	**T**$_{psc}$ **@P**$_{in}$	**Re**
	[^{o}C]	**[bar]**	**[^{o}C]**	
Tin1	30.2	74.88	31.7	9526
Tin2	34.7	74.8	31.6	21667
Tin3	44	74.41	31.4	23857
Tin4	54.5	74.38	31.4	24570
Tin5	60.2	74.59	31.5	24139

Similar conclusion can also be drawn from variation of buoyancy parameters Bu$_j$ and Ri, both of which decrease in value drastically away from pseudocritical temperature. This is shown in Figure 5.17. It is important to note that scale on Y axis for these plots is logarithmic highlighting drastic decrease in parameter values away from pseudocritical point.

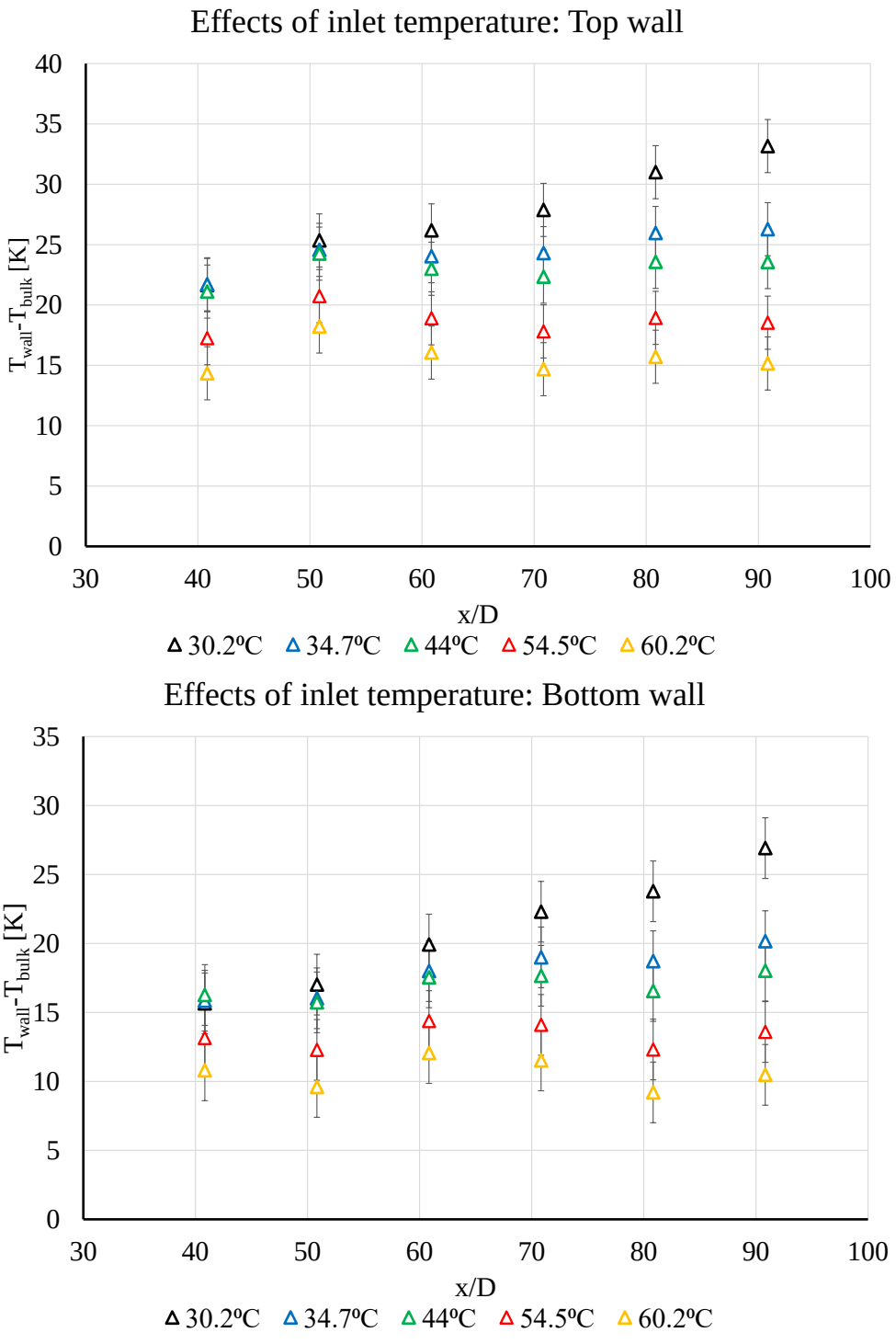

Figure 5.15: Difference between wall temperature and bulk temperature at different inlet temperature conditions

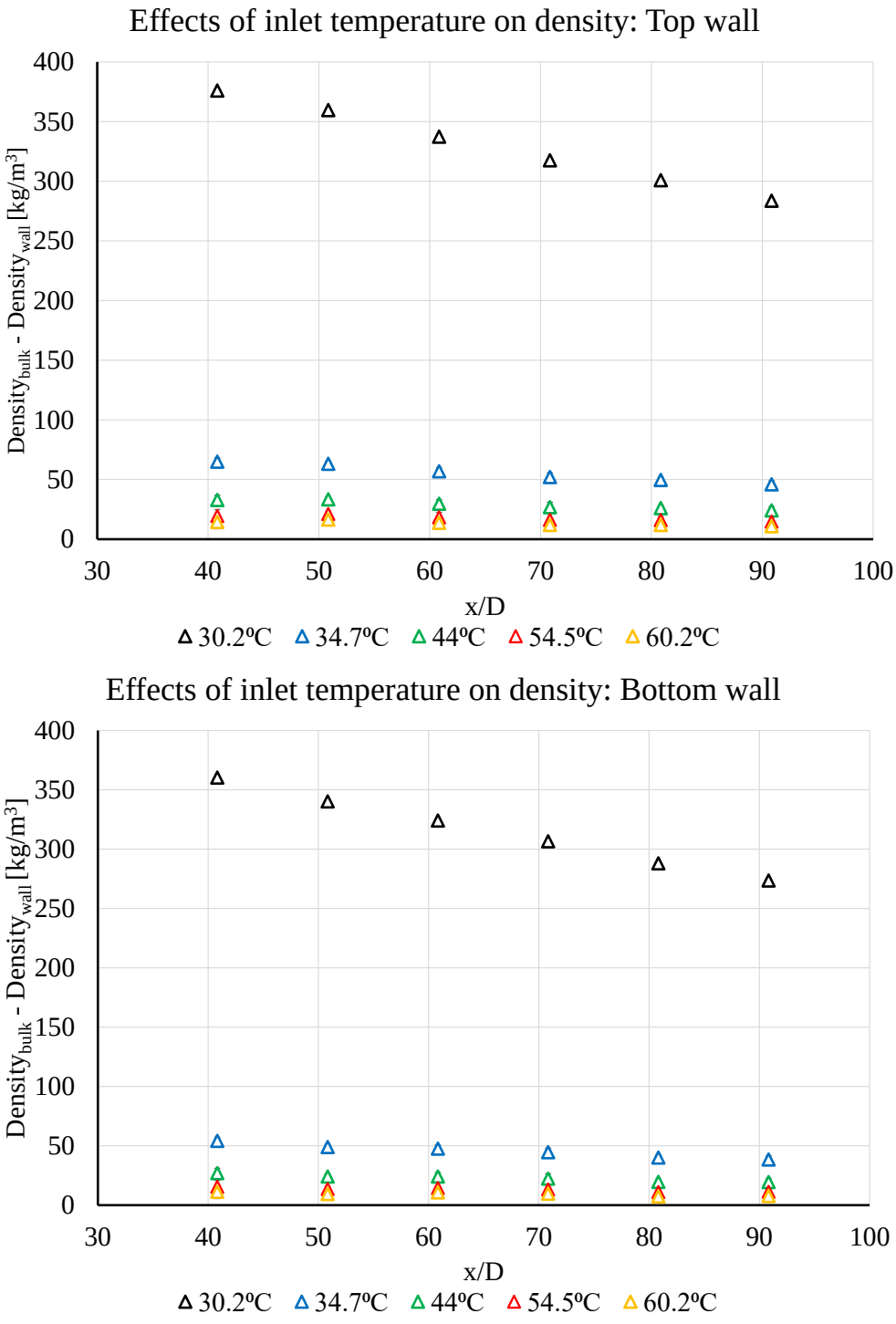

Figure 5.16: Difference between density at wall and bulk fluid density at different inlet temperature conditions

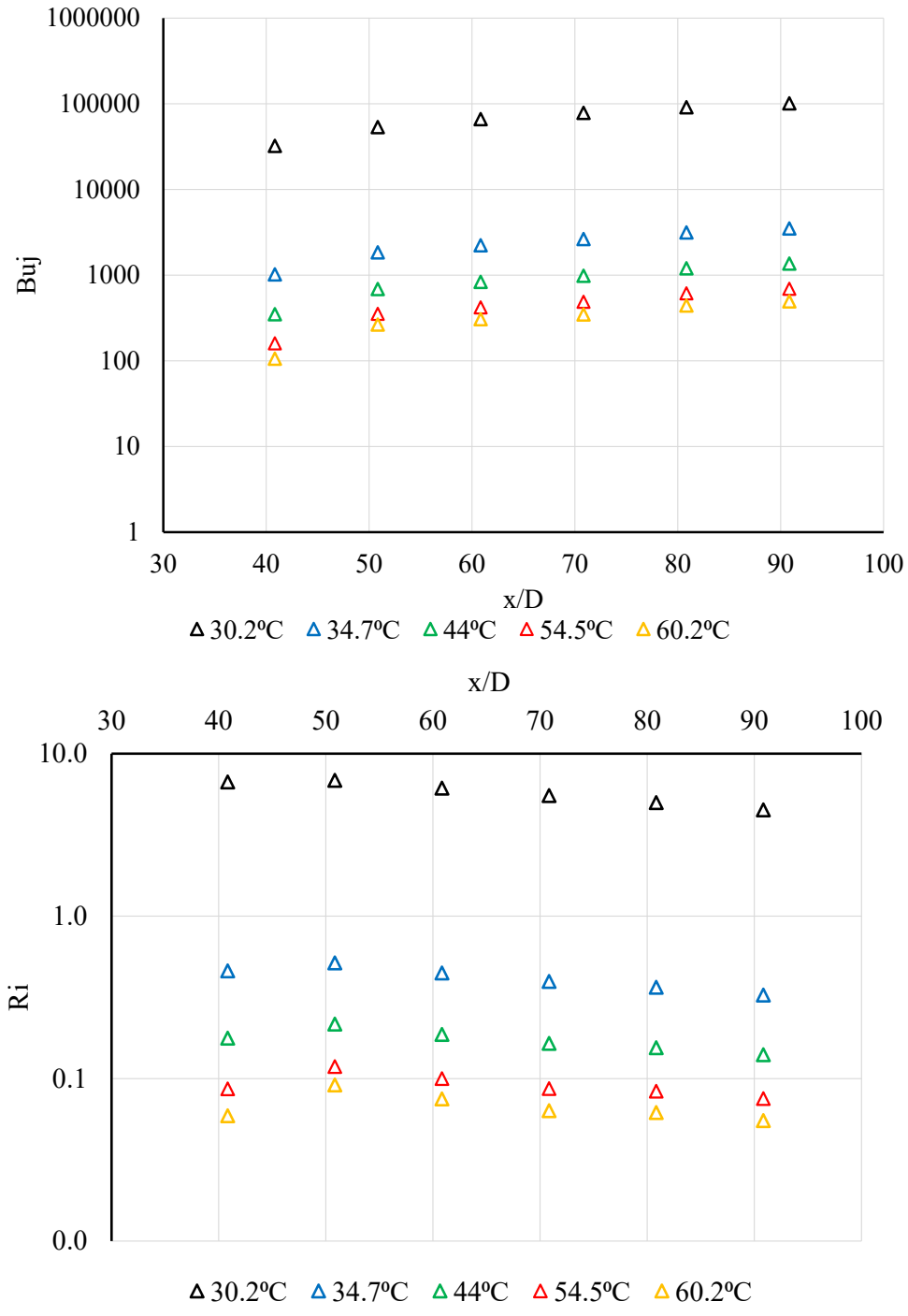

Figure 5.17: Buoyancy parameters at top wall with varying inlet temperature conditions

Buoyancy parameters

Richardson number, Ri and Jackson buoyancy parameters Bu_j are plotted alongside variation of normalized Nusselt number for all cases. Since both parameters include wall as well as bulk properties as shown in Equations 5.7 and 5.8, different wall locations have different values for these parameters. Thresholds of Ri and Bu_j appear to be applicable to determine the presence of buoyancy effects.

For varying mass flux cases, both buoyancy parameters are also observed to decrease with increase in mass flux at all wall locations. This is mainly because with increase of mass flux, forced convection overpowers natural convection. This is in agreement with the trend observed in Figure 5.8 which shows effects of buoyancy decrease with mass flux.

For increasing heat flux with constant mass flux, it is expected that natural convection become more effective while forced convection remains same. This is observed in heat transfer as shown in Figure 5.12 where the difference between bottom wall Nusselt number and top wall Nusselt number increases with increasing heat flux. However, both buoyancy parameters are observed to decrease with increase in heat flux as seen in Figure 5.14 and Figure 5.13. Similar disagreement in case of these two buoyancy parameter variation with heat flux is also reported by Kim et. al. [22] and Tanimizu & Sadr [33].

For varying bulk inlet temperature, highest value of buoyancy parameters are observed for Tin1 case where $T_{bulk} \approx <$ Tpcs as shown in Figure 5.17. For Tin1 case, the values of buoyancy parameters are significantly higher than rest of the cases. It can be estimated that at temperatures further away from pseudocritical temperatures, the values of buoyancy parameters will continue to decrease below threshold criterion for buoyancy.

Supercritical CO_2 heat transfer correlations

Table 5.5 lists previous studies with heat transfer correlations developed for either supercritical CO_2 or water in heating mode. Majority of the studies include heat transfer in vertical flow orientation with exception of Liao & Zhao [61] and Guo et al. [62]. Correlations given by Krasnoshchekov & Protopopov [63] and Krasnoshchekov [64] are in the form of Gnielinski correlation whereas all other correlations are derived form of Dittus-Boelter correlation. Range for ratio of heat flux to mass flux for this study is 35-240 J/kg. However, for this study, actual values of heat flux and mass flux are considerably lower than the studies listed in Table 5.5. For comparison, a total of 312 experimental Nusselt numbers are compared with Nusselt numbers calculated using correlations listed in Table 5.5. These 312 experimental Nusselt numbers include Nusselt numbers at all four wall locations: top, left, bottom and right. Nusselt number from correlations mainly require bulk flow properties. however, whenever required, wall properties are used according to the corresponding circumferential location. Below are the various correlations that are used here:

- Krasnoshchekov–Protopopov [63]

$$Nu_b = \frac{(f/8)Re_b Pr_b}{1.07 + 12.7\sqrt{(f/8)}(Pr_b^{2/3} - 1)} \left(\frac{\mu_w}{\mu_b}\right)^{-0.11} \left(\frac{\lambda_w}{\lambda_b}\right)^{0.33} \left(\frac{\overline{c}_p}{c_{p,b}}\right)^{0.35} \tag{5.10}$$

where,

$$f = (1.82 log Re_b - 1.64)^{-2}$$

Table 5.5: Available heat transfer correlations for sCO_2 for cases where $T_w > T_{bulk}$

Year	Author	Inclination	Testing conditions	q/G [J/kg]	Correlation
1959	Krasnoshchekov -Protopopov [63]	Vertical	10.35-10.75 MPa, 4.08 mm		5.10 [1]
1966	Krasnoshchekov [64]	Vertical	7.8-12.0 MPa, 2.22 mm, 235-500 kW/m^2		5.11 [2]
1975	Jackson-Fewster [65]	Vertical	7.6 MPa, 30-330 kW/m^2, 50-460 kg/m^{2}s	65-6600	5.12 [3]
2002	Jackson [66]	Vertical	7.25-8.27 MPa, 19.05 mm, 100-560 kW/m^2		5.13 [4]
2002	Liao-Zhao [61]	Horizontal	7.4-12 MPa, 0.7-2.16 mm, 10-200 kW/m^2	0.08-3.1	5.14
2009	Mokry et al. [67]	Vertical	7.57-8.8 MPa, 8 mm, 9-617 kW/m^2, 706-3169 kg/m^{2}s	2.8-873	5.15
2013	Gupta et al. [19]	Vertical	7.4-8.8 MPa, 15-615 kW/m^2, 900-3000 kg/m^{2}s	39-92	5.16
2008	Kim et al. [68]	Vertical	7.75-8.85 MPa, 150-500 kW/m^2, 400-1200 kg/m^{2}s	5-685	5.17
2009	Bae-Kim [69]	Vertical	7.75-8.86 MPa, 4.4-9 mm, 150 kW/m^2, 400-1200 kg/m^{2}s	125-375	5.18
2010	Kim-Kim [70]	Vertical	7.46-10.26 MPa, 4.5 mm, 38-234 kW/m^2, 208-874 kg/m^{2}s	125-375	5.19
2017	Liu et al. [71]	Vertical	7.4-10.6 MPa, 6-10 mm, 5-296 kW/m^2, 292-1507 kg/m^{2}s	43-1125	5.20
2020	Guo et al. [62]	Horizontal	7.6-8.4 MPa, 2 mm, 100-200 kW/m^2, 400-700 kg/m^{2}s	3-1013	5.21

1, 2, 3, 4- as given by Gou et al. [62]

- Krasnoshchekov [64]

$$Nu_b = \frac{(f/8)Re_b Pr_b}{1.07 + 12.7\sqrt{(f/8)}(Pr_b^{2/3} - 1)} \left(\frac{\rho_w}{\rho_b}\right)^{0.3} \left(\frac{\overline{c}_p}{c_{p,b}}\right)^n \tag{5.11}$$

where n =

$$\begin{cases} 0.4 & \text{for } T_b < T_w < T_{pc} \text{ or } 1.2T_{pc} < T_b < T_w \\ 0.4 + 0.2(T_w/T_{pc} - 1) & \text{for } T_b < T_{pc} < T_w \\ 0.4 + 0.2(T_w/T_{pc} - 1)[1 - 5(T_b/T_{pc} - 1)] & \text{for } T_{pc} < T_b < 1.2T_{pc} \end{cases}$$

- Jackson–Fewster [65]

$$Nu_b = 0.0183 Re_b^{0.82}\ \overline{Pr}_b^{0.5} \left(\frac{\rho_w}{\rho_b}\right)^{0.3} \tag{5.12}$$

- Jackson [66]

$$Nu_b = 0.0183 Re_b^{0.82}\ Pr_b^{0.5} \left(\frac{\rho_w}{\rho_b}\right)^{0.3} \left(\frac{\overline{c}_p}{c_{p,b}}\right)^n \tag{5.13}$$

where n is the same as correlation by Krasnoshchekov in Equation 5.11.

- Liao–Zhao [61]

$$Nu_b = 0.124 Re_b^{0.8}\ Pr_b^{0.4} \left(\frac{Gr}{Re_b^2}\right)^{0.203} \left(\frac{\rho_w}{\rho_b}\right)^{0.842} \left(\frac{\overline{c}_p}{c_{p,b}}\right)^{0.384} \tag{5.14}$$

where,

$$Gr = \frac{(\rho_b - \rho_w)\rho_b g d_i^3}{\mu_b^2}$$

- Mokry et al. [67]

$$Nu_b = 0.0121 Re_b^{0.86}\ \overline{Pr}_b^{0.23} \left(\frac{\rho_w}{\rho_b}\right)^{0.59} \tag{5.15}$$

- Gupta et al. [19]

$$Nu_b = 0.01 Re_b^{0.89}\ \overline{Pr}_b^{0.14} \left(\frac{\rho_w}{\rho_b}\right)^{0.93} \left(\frac{\lambda_w}{\lambda_b}\right)^{0.22} \left(\frac{\mu_w}{\mu_b}\right)^{-1.13} \tag{5.16}$$

- Kim et al. [68]

$$Nu_b = 0.0182 Re_b^{0.824}\ \overline{Pr}_b^{0.515} \left(\frac{\rho_w}{\rho_b}\right)^{0.299} \tag{5.17}$$

- Bae–Kim [69]

$$Nu_b = 0.021 Re_b^{0.82}\ Pr_b^{0.5} \left(\frac{\rho_w}{\rho_b}\right)^{0.3} \left(\frac{\overline{c}_p}{c_{p,b}}\right)^{n} f(Bu) \tag{5.18}$$

where,

$$Bu = \frac{\overline{Gr}_b}{Re_b^{2.7}\overline{Pr}_b^{0.5}}$$

where f(Bu) =

$$\begin{cases} (1+10^8 Bu)^{-0.032} & \text{when } 5\times10^{-8} < Bu < 7\times10^{-7} \\ 0.0185 Bu^{-0.43465} & \text{when } 7\times10^{-7} < Bu < 1\times10^{-6} \\ 0.75 & \text{when } 1\times10^{-6} < Bu < 1\times10^{-5} \\ 0.0119 Bu^{-0.36} & \text{when } 1\times10^{-5} < Bu < 3\times10^{-5} \\ 32.4 Bu^{0.4} & \text{when } 3\times10^{-5} < Bu < 1\times10^{-4} \end{cases}$$

- Kim–Kim [70]

$$Nu_b = 0.226 Re_b^{1.174}\ Pr_b^{1.057} \left(\frac{\rho_w}{\rho_b}\right)^{0.571} \left(\frac{\overline{c}_p}{c_{p,b}}\right)^{1.032} Ac^{0.489} Bu^{0.0021} \tag{5.19}$$

where,

$$Ac = \frac{q\beta_b}{G c_{p,b} Re_b^{0.625}} \left(\frac{\rho_w}{\rho_b}\right)^{0.5} \left(\frac{\mu_w}{\mu_b}\right)$$

where,

$$Bu = \frac{Gr}{Re_b^{3.425} Pr_b^{0.8}} \left(\frac{\rho_w}{\rho_b}\right)^{0.5} \left(\frac{\mu_w}{\mu_b}\right)$$

- Liu et al. [71]

$$Nu_b = 0.00075 Re_b^{0.93} \overline{Pr}_b^{0.68} \left(\frac{\rho_w}{\rho_b}\right)^{0.42} exp(Ac^{0.079}) exp(Bu^{-0.023})[1 + 2.63/(L/d_i)] \quad (5.20)$$

where,

$$Ac = \frac{4q\beta_b}{Gc_{p,b}Re_b^{0.625}} \left(\frac{\rho_w}{\rho_b}\right)^{-0.5} \left(\frac{\mu_w}{\mu_b}\right)$$

where,

$$Bu = \frac{Gr}{Re_b^{2.625} Pr_w^{0.4}} \left(\frac{\rho_w}{\rho_b}\right)^{-0.5} \left(\frac{\mu_w}{\mu_b}\right)$$

- Guo [62]

$$Nu_b = 0.114 Re_b^{0.589} \overline{Pr}_b^{0.465} \left(\frac{Gr}{Re_b^2}\right)^{-0.125} \left(\frac{\rho_w}{\rho_b}\right)^{0.240} \left(\frac{\overline{c}_p}{c_{p,b}}\right)^{0.096} \quad (5.21)$$

Discrepancies among available heat transfer correlations

Before comparing experimental Nusselt number from this study to Nusselt number obtained from available correlations, it is important to investigate how do Nusselt numbers calculated from these correlations compare among themselves. Correlations given by studies listed in Table 5.5 vary based on different parameters used and exponents of wall-to-bulk property ratios. In addition to that, these studies were performed at different testing conditions. All of this results in disagreement among Nusselt number obtained from their correlations.

For this purpose, most recent correlation given by Gou et al. [62] is compared with four other correlations given by Jackson [66], Liao & Zhao [61], Gupta et al. [19] and Bae & Kim [69]. Difference in Nusselt numbers is plotted against ratio of bulk temperature to pseudocritical temperature in Figures 5.18 and 5.19 as follows:

$$\frac{Nu_{model} - Nu_{Guo}}{Nu_{Guo}} \times 100\% \tag{5.22}$$

Figures 5.18 and 5.19 show large disagreement among the different correlations. In fact, Guo et al. [62] themselves have reported similar disagreement. There can be a few reasons behind the agreement: (1) The parameters used in these correlations may not be enough to represent the full physics and additional parameters may be necessary. (2) Heat transfer coefficient is a local similarity variable that is the constant of proportionality between local heat flux and local driving temperature difference. Majority of the correlations are developed based on a global individual averages of heat flux, wall temperature and fluid bulk temperature, which is not consistent with the Newton's law of cooling. With this in mind, following subsection discusses comparison of experimental Nusselt number from this study with Nusselt number calculated from available correlations.

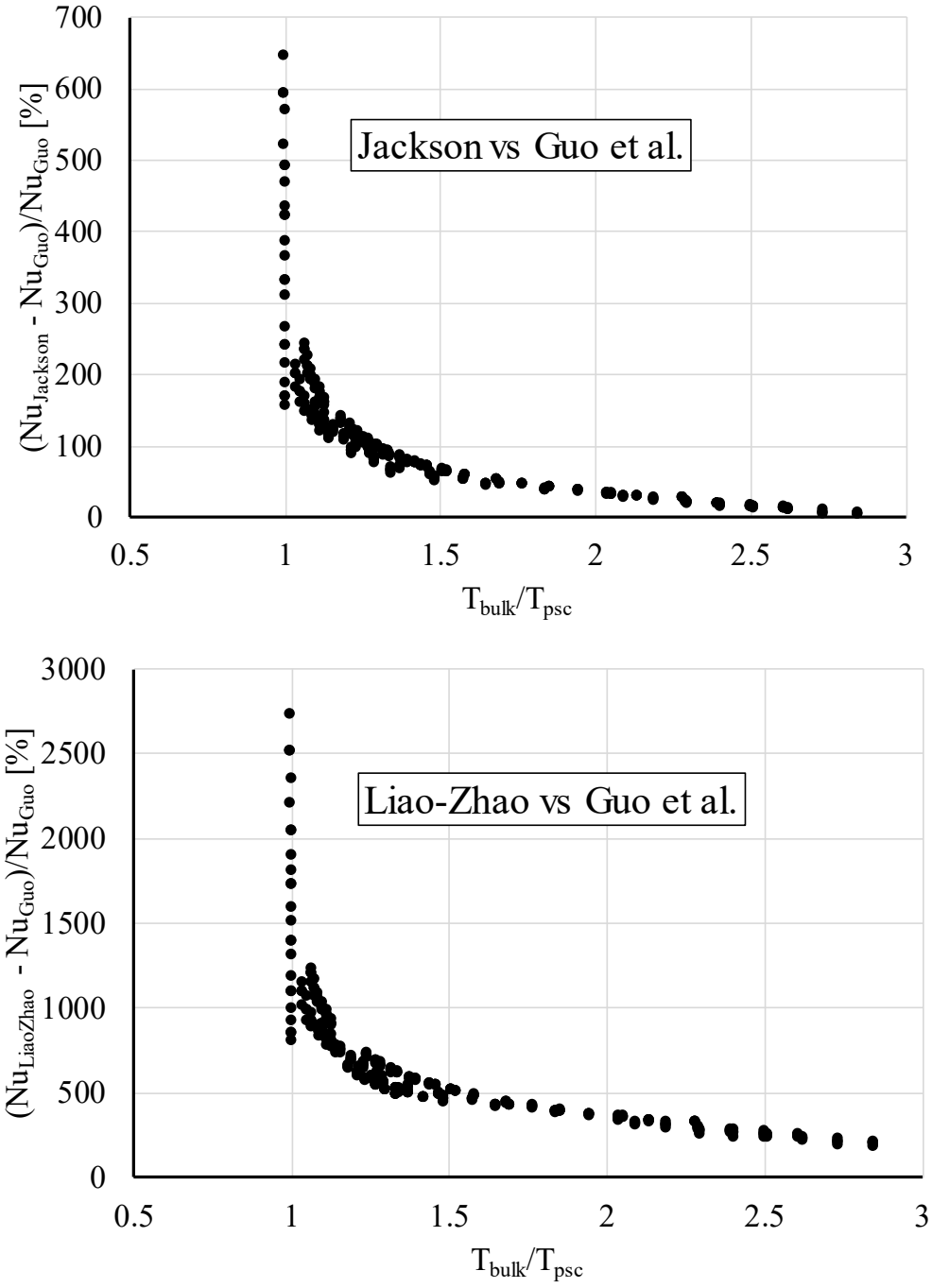

Figure 5.18: Discrepancies among available sCO_2 correlations

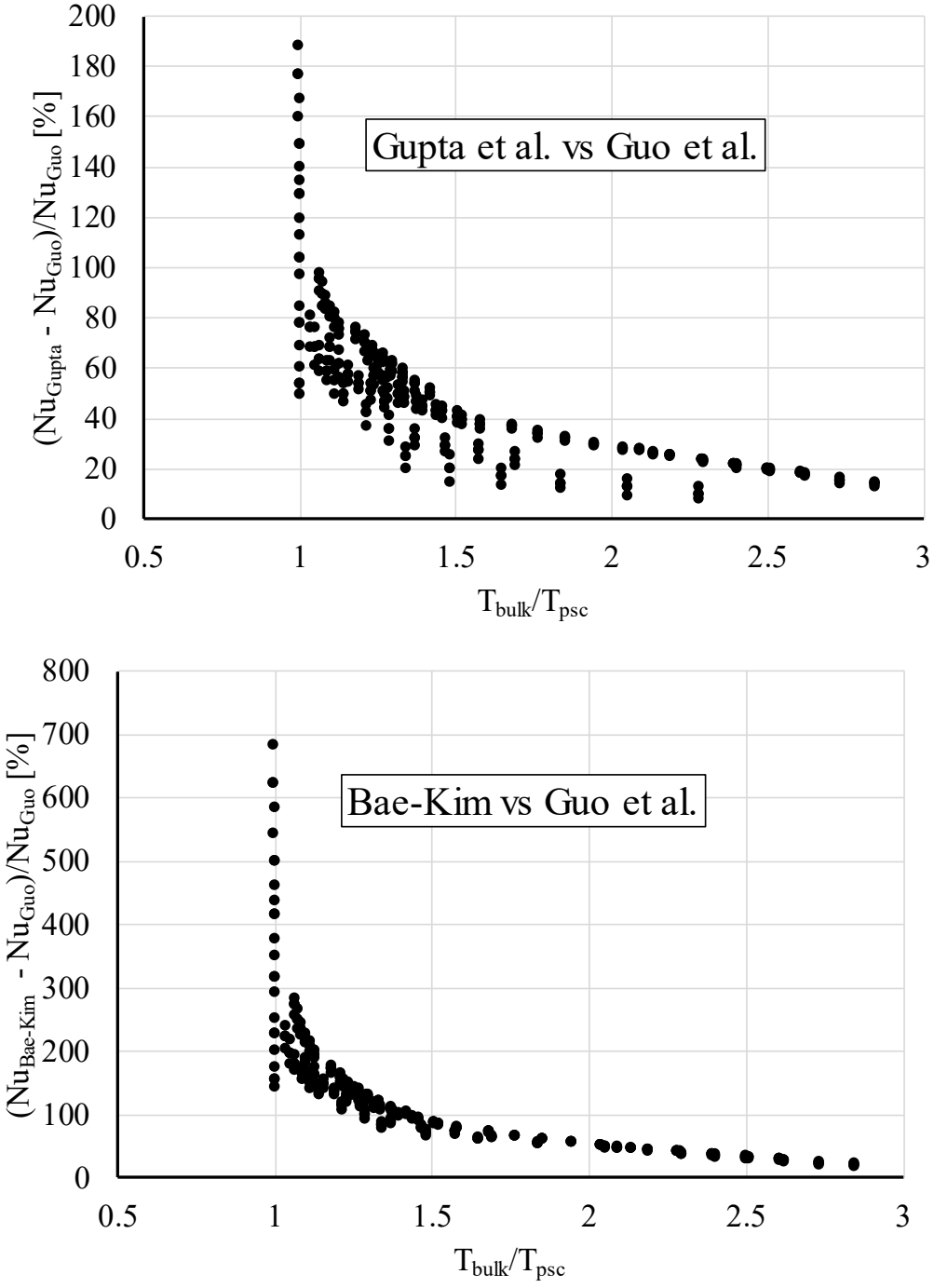

Figure 5.19: Continued- Discrepancies among available sCO_2 correlations

Comparison of experimental data to available heat transfer correlations

Error in calcualted Nusselt numbers from correlations and from experiments are plotted against ratio of bulk temperature to pseudocritical temperature. These plots are shown in Figure 5.20, 5.21, 5.22, 5.23, 5.24 and 5.25. From the results, it can be seen that available correlations cannot well predict the heat transfer for low heat flux and low mass flux conditions used in this study. Most of the over-prediction of heat transfer occurs very close to pseudocritical temperature compared to away from pseudocritical temperature. Under-prediction and over-prediction of heat transfer is closely related to the testing conditions such as mass flux and heat flux; specifically ratio of heat flux to mass flux. Correlations which are developed using studies with lower value of this ratio, tend to over-predict heat transfer and vice versa. For current study, range for ratio of heat flux to mass flux is 35-240 J/kg. Study by Liao & Zhao [61] is one of first to include Richardson number (Gr/Re^2) as a correction term for horizontal flows. They reported increased heat transfer near pseudocritical temperature for horizontal flows. Correlations given by Liao & Zhao with $(q/G)_{max}$ of 3.1 J/kg, over-predicts heat transfer for most of the cases. Correlations given by Liu et al. [71] and Guo et al. [62] with $(q/G)_{max}$ of 1125 J/kg and 1013 J/kg, respectively, under-predicts heat transfer for most of the cases.

All of the correlations discussed here include some form of ratio of wall to bulk properties with exponent based on experimental results. Values of these exponents depend highly on testing conditions such as pipe diameter, mass flux and heat flux. This means that all of the correlations are very sensitive to their respective testing conditions. ***One correlation alone may not be able to predict heat transfer accurately all the time. At least close to the critical point where property variations are significant, a possible solution to this dilemma is to develop multiple correlations for different regimes of pipe sizes, heat flux and mass flux.***

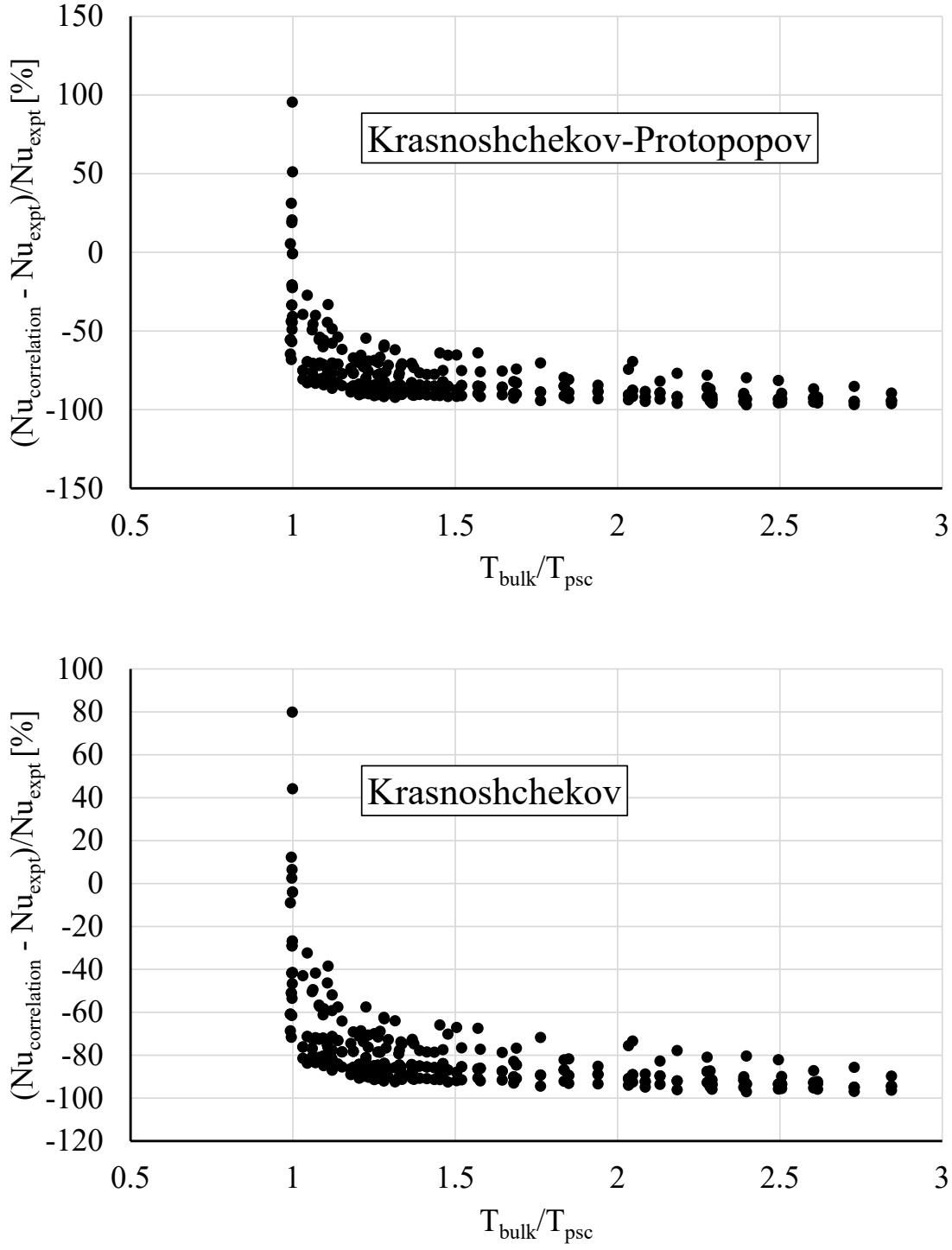

Figure 5.20: Error in predicting Nusselt number from available sCO_2 correlations

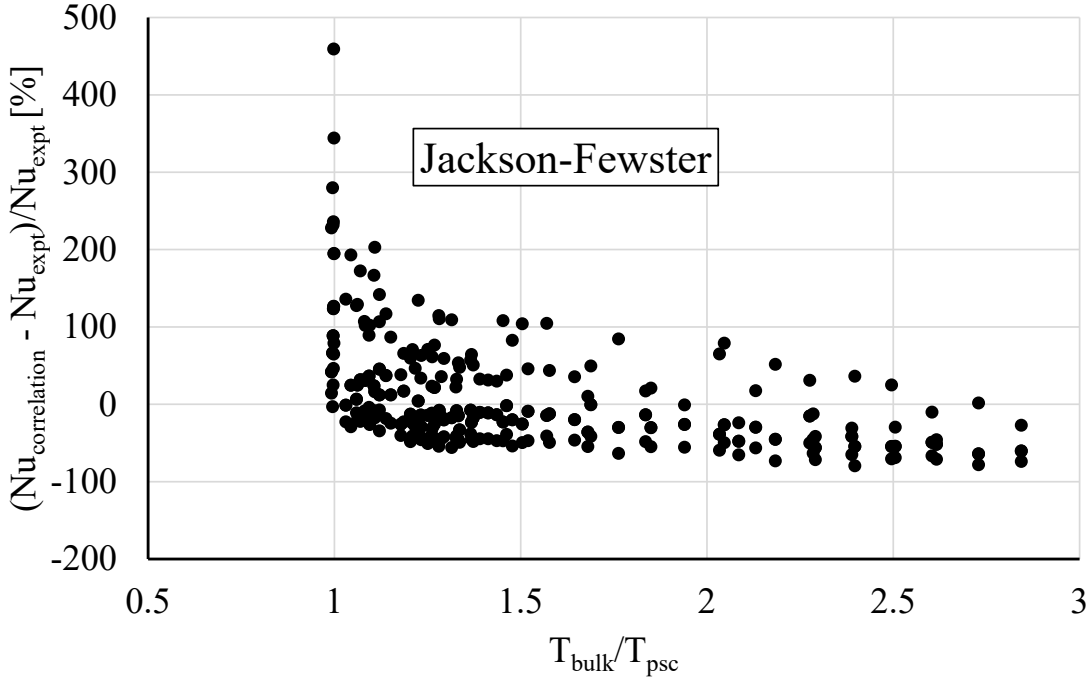

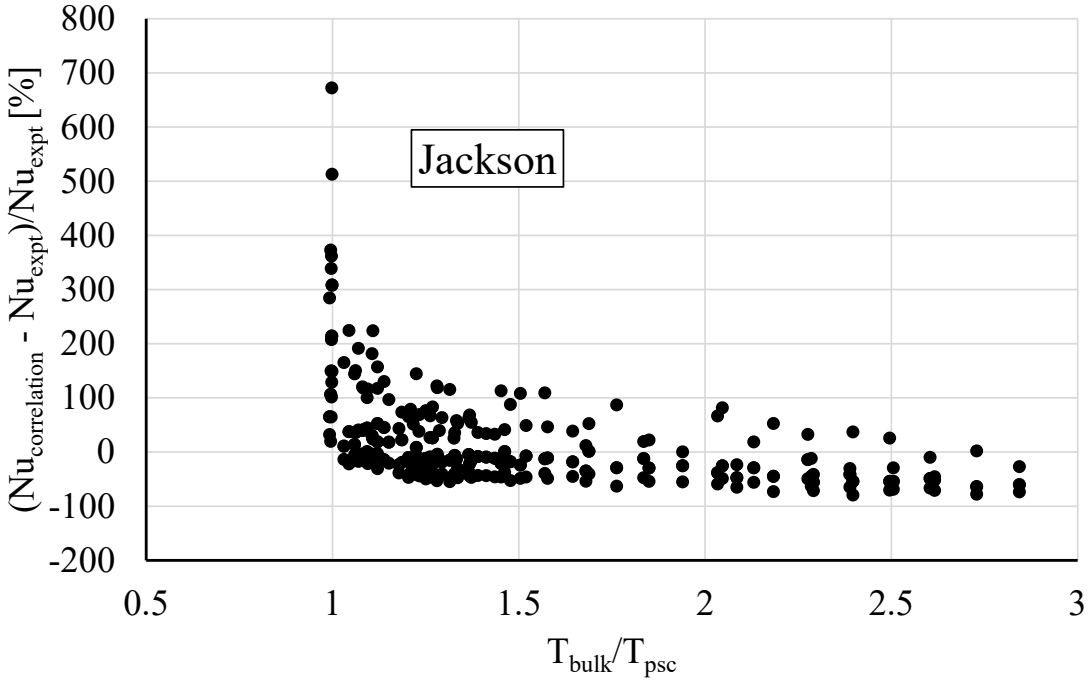

Figure 5.21: Continued- Error in predicting Nusselt number from available sCO_2 correlations

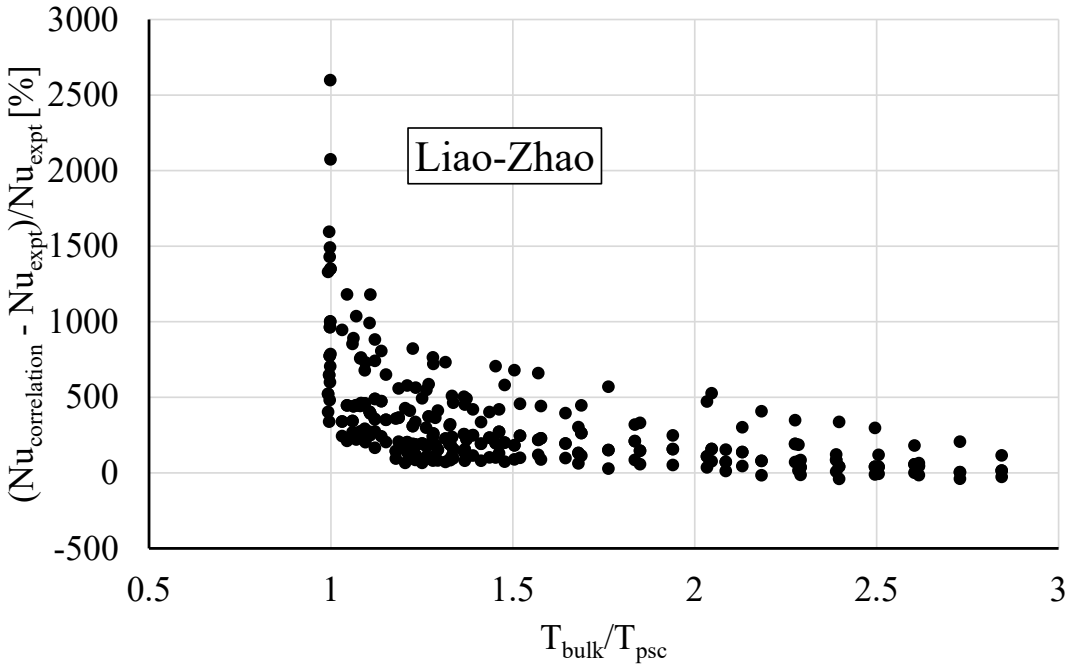

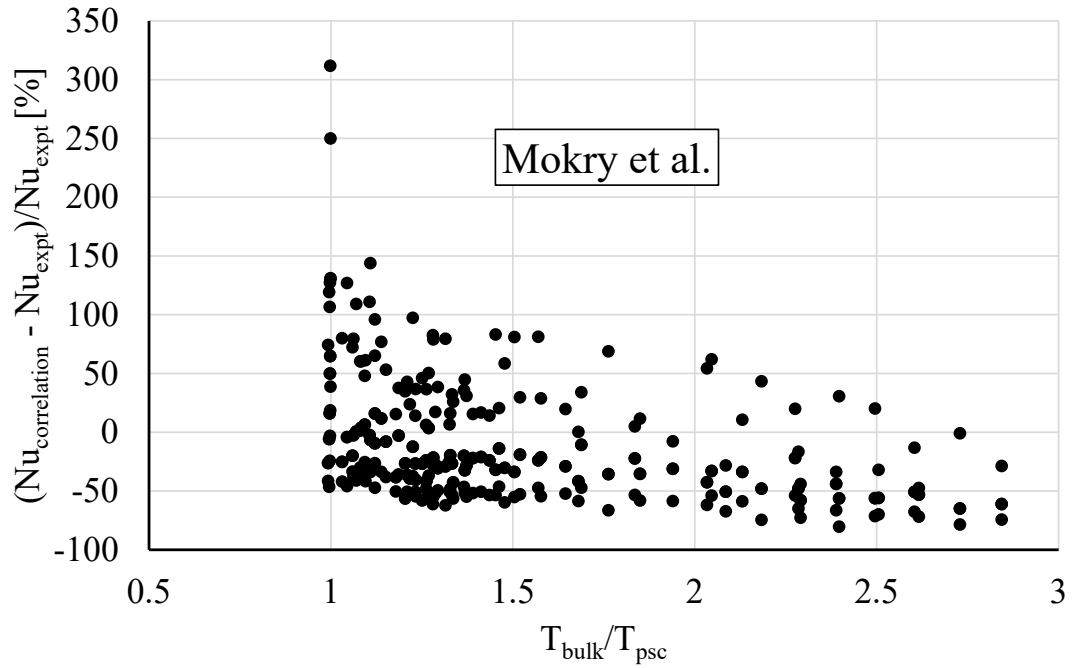

Figure 5.22: Continued- Error in predicting Nusselt number from available sCO_2 correlations

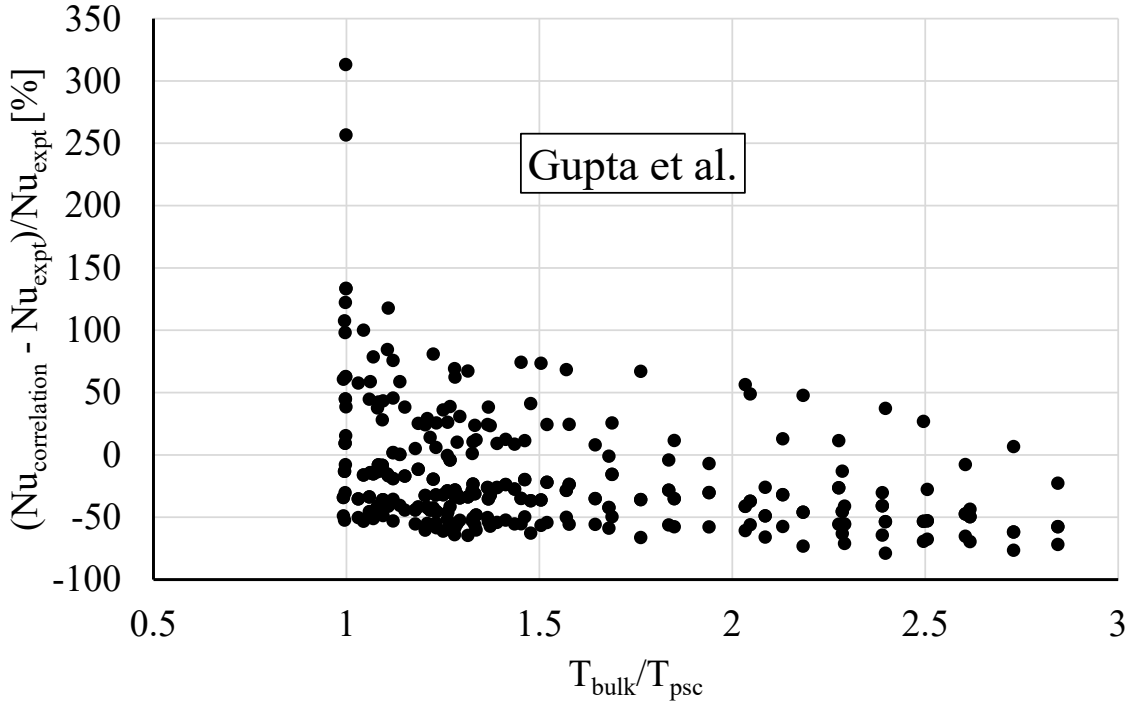

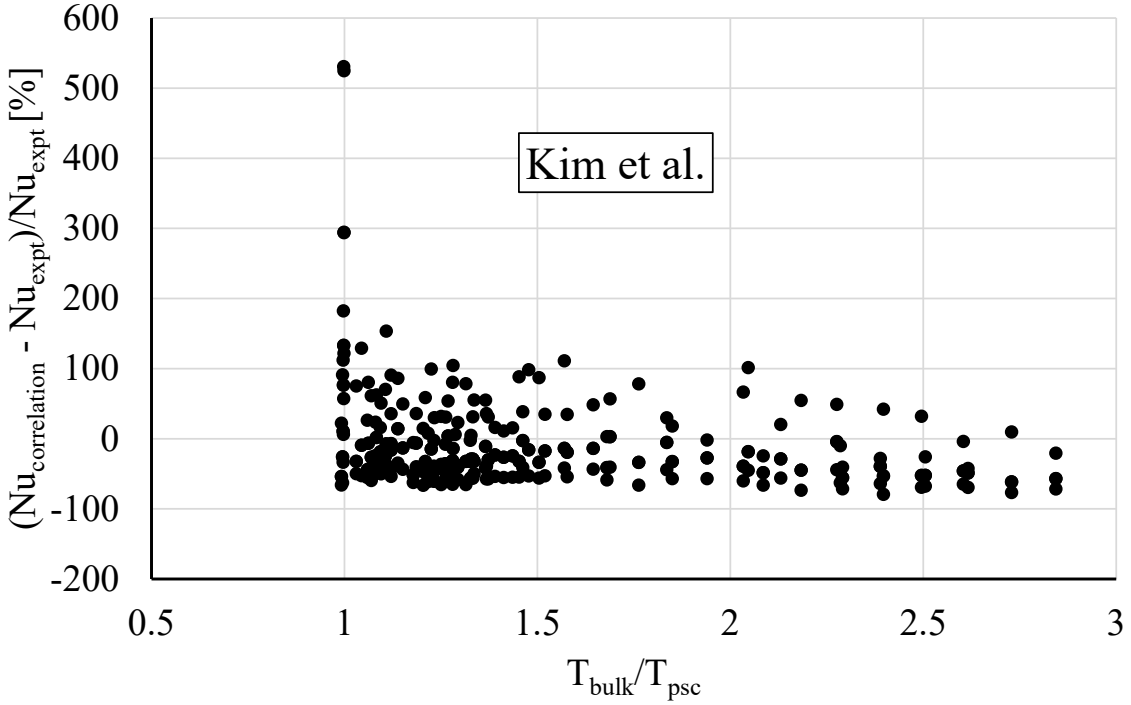

Figure 5.23: Continued- Error in predicting Nusselt number from available sCO_2 correlations

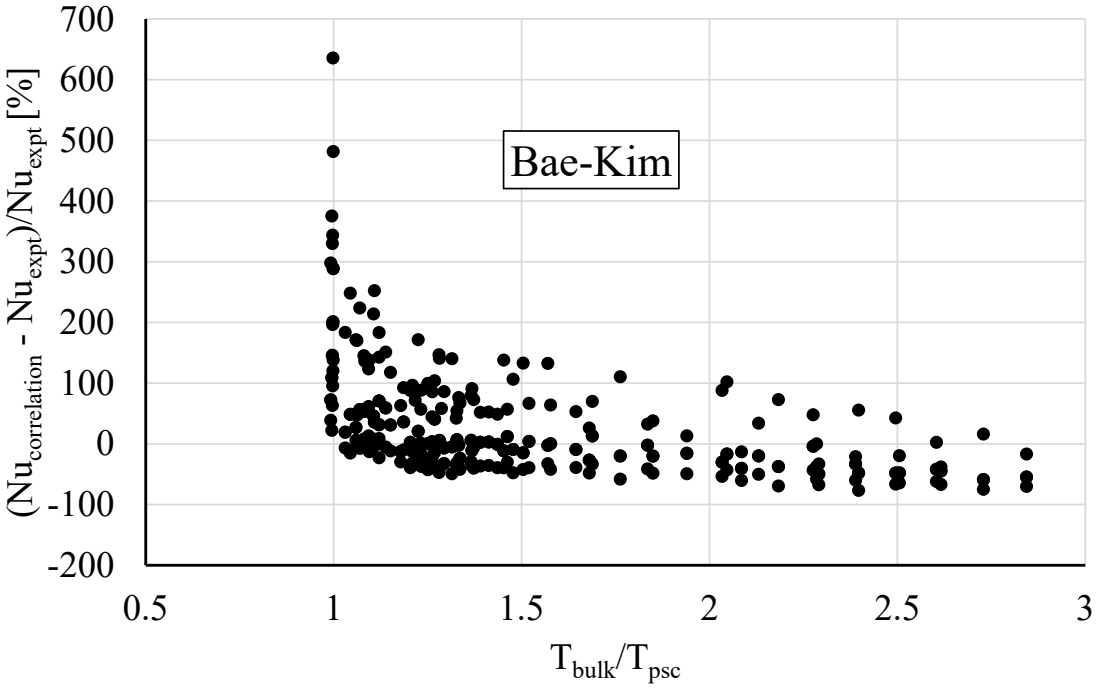

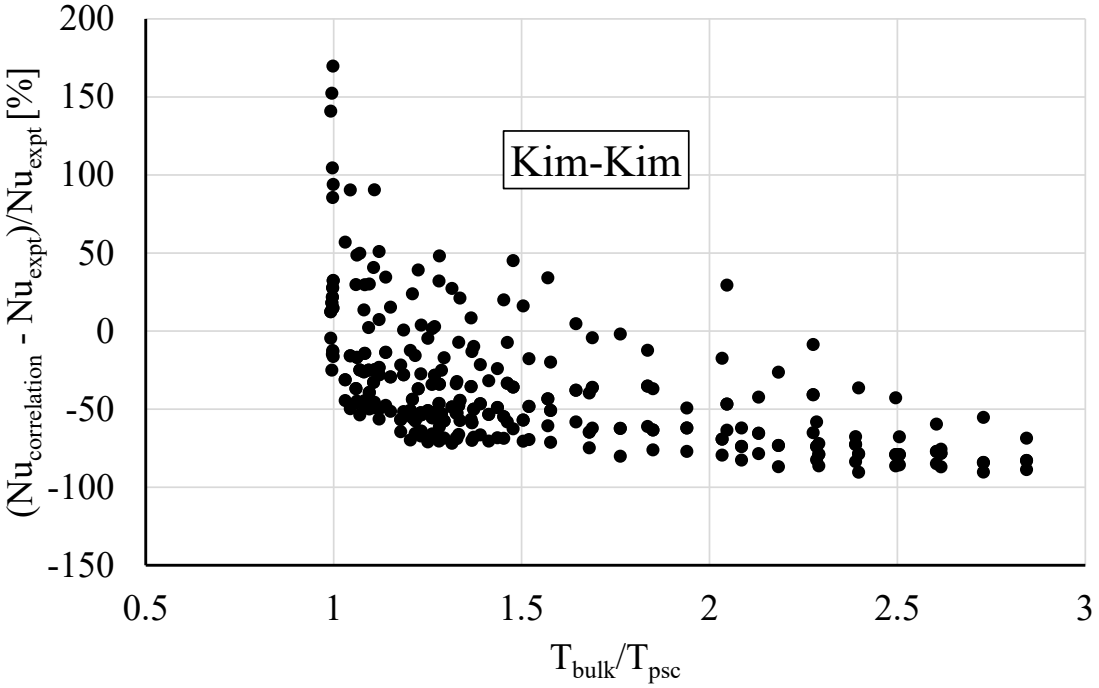

Figure 5.24: Continued- Error in predicting Nusselt number from available sCO_2 correlations

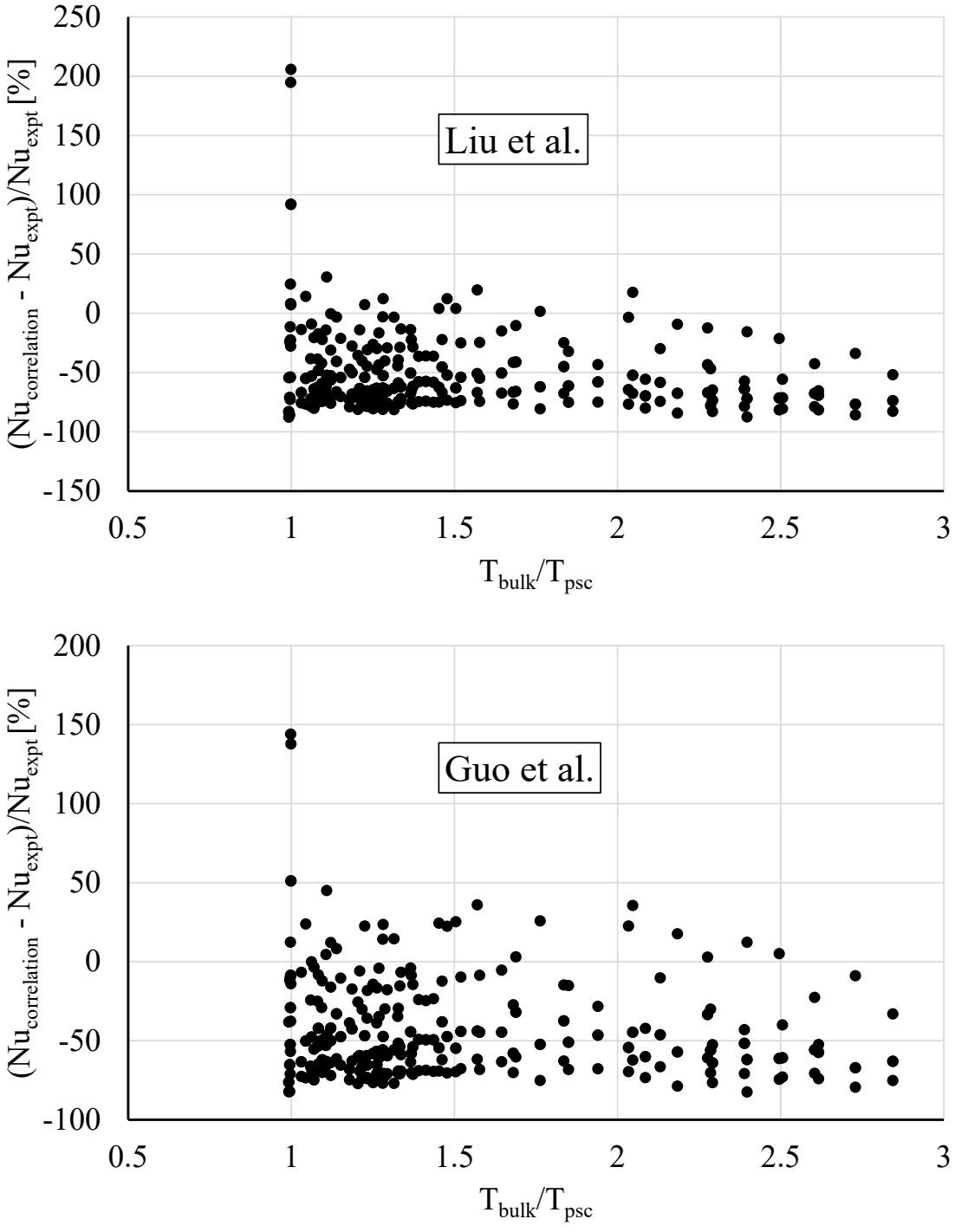

Figure 5.25: Continued- Error in predicting Nusselt number from available sCO_2 correlations

CHAPTER 6: CONCLUSIONS

Heat transfer experiments are performed to investigate effects of different testing conditions for supercritical CO_2 (sCO_2) flow in circular horizontal tube in heating mode. Validation of the experimental setup has been carried out with high pressure air heat transfer experiments. Nusselt number from air validation cases show good agreement within 10% of conventional Dittus-Boelter and Gnielinski Nusselt numbers. For sCO_2 experiments the region of interest was near critical point with pressure ≈ 74.5 bar with varying testing conditions. Variable parameters studied here are inlet mass flux, heat flux and bulk flow inlet temperature. To study the effects of each parameter, remaining two parameters are kept constant. Below are the summarized conclusions.

- For all the cases studied, effects of buoyancy on heat transfer are apparent given the difference in Nusselt number values between top, bottom and side wall. Highest Nusselt numbers are observed at the bottom walls where upward convective currents aid heat transfer.
- Nusselt numbers at the side wall were always in between Nusselt numbers at top and bottom walls.
- Buoyancy effects increase with increase in heat flux and decrease in mass flux.
- Buoyancy effects start to disappear away from pseudocritical temperature.
- Richardson number and Jackson buoyancy parameter perform well as threshold criterion for buoyancy but do not match with trend and magnitude of effects of buoyancy.
- Performance of heat transfer correlations available in literature depends highly on their original testing conditions. One correlation alone will not be able to predict

heat transfer accurately. At least close to the critical point where property variations are significant, different correlations for different regimes of pipe diameter, heat flux and mass flux may provide possible solution for this problem.

Future work

Open loop experimental setup emphasized inability to test higher mass flux and higher heat flux conditions. Future work will include include setup of closed loop experimental facility which will be able to span wide range of heat flux and mass flux. Future work will also include performing systematic experiments with different testing conditions such as pipe diameter, heat flux and mass flux. Based on such systematic experiments, heat transfer correlations will be developed based on different regimes of pipe diameter, heat flux and mass flux.

APPENDIX A: ADDITIONAL TEST RESULTS

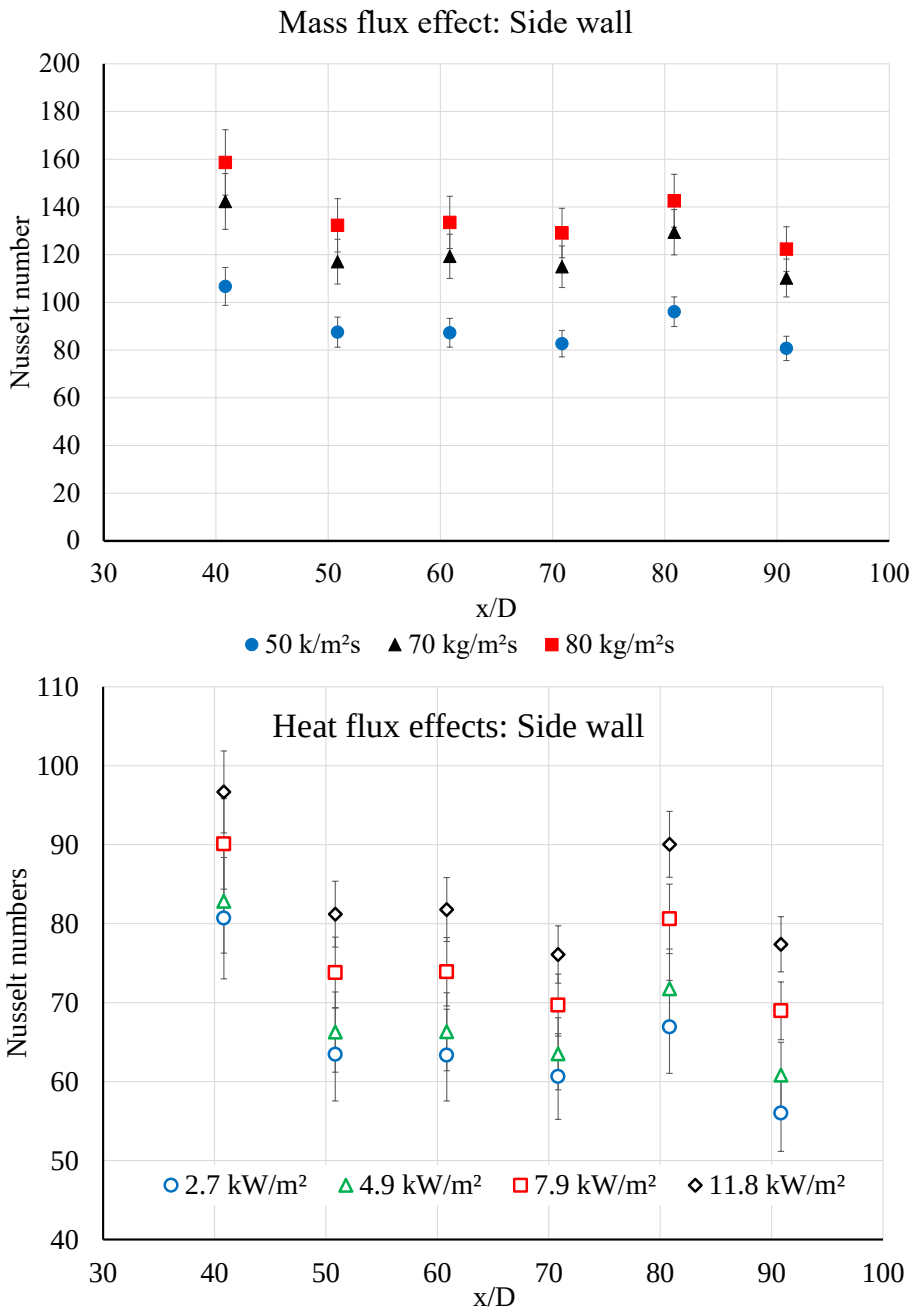

Figure A.1: Nusselt numbers at side wall location: Top- variation with mass flux, Bottom- variation with heat flux

LIST OF REFERENCES

[1] Khadse, A., Blanchette, L., Kapat, J., Vasu, S., Hossain, J., and Donazzolo, A., 2018. "Optimization of supercritical co2 brayton cycle for simple cycle gas turbines exhaust heat recovery using genetic algorithm". *Journal of Energy Resources Technology,* ***140***(7).

[2] (US), E. I. A., and Office, G. P., 2016. *International Energy Outlook 2016, with Projections to 2040*. Government Printing Office.

[3] Rathi, A., 2018. A radical us startup has successfully fired up its zero-emissions fossil-fuel power plant https://qz.com/1292891/net-powers-has-successfully-fired-up-its-zero-emissions-fossil-fuel-power-plant/.

[4] Dostal, V., Hejzlar, P., and Driscoll, M. J., 2006. "High-performance supercritical carbon dioxide cycle for next-generation nuclear reactors". *Nuclear Technology,* ***154***(3), pp. 265–282.

[5] Turchi, C. S., Ma, Z., and Dyreby, J., 2012. "Supercritical carbon dioxide power cycle configurations for use in concentrating solar power systems". In ASME Turbo Expo 2012: Turbine Technical Conference and Exposition, American Society of Mechanical Engineers Digital Collection, pp. 967–973.

[6] Mohagheghi, M., and Kapat, J., 2013. "Thermodynamic optimization of recuperated s-co2 brayton cycles for solar tower applications". In ASME Turbo Expo 2013: Turbine Technical Conference and Exposition, American Society of Mechanical Engineers Digital Collection.

[7] Dostal, V., Driscoll, M. J., and Hejzlar, P., 2004. "A supercritical carbon dioxide cycle for next generation nuclear reactors". PhD thesis, Massachusetts Institute of Technology, Department of Nuclear Engineering.

[8] Siemens Energy, 2017. Sgt6-8000h heavy-duty gas turbine (60hz) https://new.siemens.com/global/en/products/energy/power-generation/gas-turbines/sgt6-8000h.html.

[9] Elson, A., Tidball, R., and Hampson, A., 2015. "Waste heat to power market assessment". *Oak Ridge, TN, United States: Building Technologies Research and Integration Center (BTRIC), Oak Ridge National Laboratory (ORNL)*.

[10] Echogen power systems, 2020. Eps100 heat recovery solution https://www.echogen.com/our-solution/product-series/eps100/.

[11] NET Power, 2020. Net power's patented thermodynamic cycle https://netpower.com/the-cycle/.

[12] National Renewable Energy Laboratory, 2020. 10 mwe supercritical-co2 turbine https://www.nrel.gov/docs/fy12osti/55455.pdf.

[13] Gas Turbine Institute, 2020. 10 mwe supercritical carbon dioxide (sco2) pilot power plant https://www.gti.energy/wp-content/uploads/2019/01/STEP-Project-Detailed-Description-Dec2018.pdf.

[14] Dang, C., and Hihara, E., 2004. "In-tube cooling heat transfer of supercritical carbon dioxide. part 1. experimental measurement". *International journal of refrigeration*, **27**(7), pp. 736–747.

[15] Dang, C., and Hihara, E., 2004. "In-tube cooling heat transfer of supercritical carbon dioxide. part 2. comparison of numerical calculation with different turbulence models". *International journal of refrigeration,* ***27***(7), pp. 748–760.

[16] Lin, W., Du, Z., and Gu, A., 2012. "Analysis on heat transfer correlations of supercritical co 2 cooled in horizontal circular tubes". *Heat and Mass Transfer,* ***48***(4), pp. 705–711.

[17] Adebiyi, G. A., and Hall, W., 1976. "Experimental investigation of heat transfer to supercritical pressure carbon dioxide in a horizontal pipe". *International journal of heat and mass transfer,* ***19***(7), pp. 715–720.

[18] Pidaparti, S. R., McFarland, J. A., Mikhaeil, M. M., Anderson, M. H., and Ranjan, D., 2015. "Investigation of buoyancy effects on heat transfer characteristics of supercritical carbon dioxide in heating mode". *Journal of Nuclear Engineering and Radiation Science,* ***1***(3), p. 031001.

[19] Gupta, S., Saltanov, E., Mokry, S. J., Pioro, I., Trevani, L., and McGillivray, D., 2013. "Developing empirical heat-transfer correlations for supercritical co2 flowing in vertical bare tubes". *Nuclear Engineering and Design,* ***261***, pp. 116–131.

[20] Lei, X., Zhang, Q., Zhang, J., and Li, H., 2017. "Experimental and numerical investigation of convective heat transfer of supercritical carbon dioxide at low mass fluxes". *Applied Sciences,* ***7***(12), p. 1260.

[21] Yang, C.-Y., and Liao, K.-C., 2017. "Effect of experimental method on the heat transfer performance of supercritical carbon dioxide in microchannel". *Journal of Heat Transfer,* ***139***(11), p. 112404.

[22] Kim, T. H., Kwon, J. G., Kim, M. H., and Park, H. S., 2018. "Experimental investigation on validity of buoyancy parameters to heat transfer of co2 at supercritical pressures in a horizontal tube". *Experimental Thermal and Fluid Science,* **92**, pp. 222–230.

[23] Jackson, J., Hall, W., Fewester, J., Watson, A., and Watts, M. Htfs design report no. 34-heat transfer to supercritical pressure fluids. part 2-critical reviews with design recommendations. uk atomic energy authority harwell. 1975.

[24] Jackson, J., 2013. "Fluid flow and convective heat transfer to fluids at supercritical pressure". *Nuclear Engineering and Design,* ***264***, pp. 24–40.

[25] Jiang, P., Zhang, Y., and Shi, R., 2006. "Experimental and numerical investigation of convection heat transfer of co2 at super-critical pressures in a vertical mini tube". In ASME 4th International Conference on Nanochannels, Microchannels, and Minichannels, American Society of Mechanical Engineers, pp. 583–590.

[26] Deshmukh, A., Kapat, J., and Khadse, A. "Transient thermodynamic modeling of air cooler in supercritical co2 brayton cycle for solar molten salt application". In ASME Turbo Expo 2019: Turbomachinery Technical Conference and Exposition, American Society of Mechanical Engineers Digital Collection.

[27] Pioro, I. L., and Duffey, R. B., 2007. *Heat transfer and hydraulic resistance at supercritical pressures in power engineering applications*. American Society of Mechanical Engineers.

[28] Koppel, L., and Smith, J., 1962. "Laminar flow heat transfer for variable physical properties".

[29] Melik-Pashaev, N., 1966. "Calculation of convective heat transfer at supercritical pressure(convective heat transfer through stabilized turbulent flow of chemically ho-

mogeneous liquid in circular pipe under supercritical pressure conditions)". *HIGH TEMPERATURE,* ***4***, pp. 789–798.

[30] Krasnoshchekov, E., Kuraeva, I., and Protopopov, V., 1969. "Local heat transfer of carbon dioxide at supercritical pressure under cooling conditions". *High Temperature,* ***7***(5), pp. 856–+.

[31] Schnurr, N., 1969. "Heat transfer to carbon dioxide in the immediate vicinity of the critical point".

[32] Krasnoshchekov, E., and Protopopov, V., 1971. Generalized relationship for calculation of heat-transfer to carbon-dioxide at supercritical pressure (pi= 1.02-5.25).

[33] Tanimizu, K., and Sadr, R., 2016. "Experimental investigation of buoyancy effects on convection heat transfer of supercritical co 2 flow in a horizontal tube". *Heat and Mass Transfer,* ***52***(4), pp. 713–726.

[34] Petukhov, B., Polyakov, A. F., Kuleshov, V., and Sheckter, Y. L., 1974. "Turbulent flow and heat transfer in horizontal tubes with substantial influence of thermogravitational forces". In International Heat Transfer Conference Digital Library, Begel House Inc.

[35] Piping, P., 2016. "Asme b31. 3". *The American Society of Mechanical Engineers*.

[36] Boyd, E. J., McClintic, J. W., Chavez, K. F., and Bogard, D. G., 2017. "Direct measurement of heat transfer coefficient augmentation at multiple density ratios". *Journal of Turbomachinery,* ***139***(1).

[37] Hossain, J., Curbelo, A., Garrett, C., Wang, W., Kapat, J., Thorpe, S., and Maurer, M., 2017. "Use of rib turbulators to enhance postimpingement heat transfer for curved surface". *Journal of Engineering for Gas Turbines and Power,* ***139***(7).

[38] Curbelo, A., Kapat, J. S., Thorpe, S. J., and Maurer, M., 2019. "Optimization of inserts to minimize cross-flow impact in impingement heat transfer". In Turbo Expo: Power for Land, Sea, and Air, Vol. 58653, American Society of Mechanical Engineers, p. V05BT18A005.

[39] Gao, Z., Wright, L. M., and Han, J.-C., 2005. "Assessment of steady state psp and transient ir measurement techniques for leading edge film cooling". In ASME 2005 International Mechanical Engineering Congress and Exposition, American Society of Mechanical Engineers Digital Collection, pp. 467–475.

[40] Tran, L. V., Pham, A. L., Little, Z. D., and Kapat, J. S., 2013. "Characterization of thermochromic liquid crystals for multi-color transient heat transfer experiments". In 44th AIAA Thermophysics Conference, p. 3012.

[41] Otto, M., 2019. "Improving turbine performance: A contribution to the understanding of heat transfer and vortical structures in staggered pin fin arrays".

[42] Ahmed, L., 2018. "Detailed understanding of flow, heat transfer, and pressure drop behavior in a square channel with 45 deg ribs".

[43] Ahmed, L., Vergos, C., Tran, P. K., Wang, W., and Kapat, J. S., 2015. "Investigation of pressure drop and heat transfer behavior of a square channel with 45 angle ribs at wide range of reynolds numbers". In 51st AIAA/SAE/ASEE Joint Propulsion Conference, p. 4131.

[44] of Mechanical Engineers, A. S., 2004. *Standard ASME B36.19M-2004: Stainless Steel Pipe*. American Society of Mechanical Engineers.

[45] Kazemifar, F., and Kyritsis, D. C., 2014. "Experimental investigation of near-critical co2 tube-flow and joule–thompson throttling for carbon capture and sequestration". *Experimental thermal and fluid science*, ***53***, pp. 161–170.

[46] Franssen, J.-M., and Real, P. V., 2012. *Fire Design of Steel Structures: Eurocode 1: Actions on structures; Part 1-2: General actions–Actions on structures exposed to fire; Eurocode 3: Design of steel structures; Part 1-2: General rules–Structural fire design*. John Wiley & Sons.

[47] Filonenko, G., 1954. "Hydraulic resistance in pipes".

[48] Mikheev, M. A., and Mikheeva, I., 1956. "Principles of heat transfer". *Gosénergoizdat, Moscow-Leningrad*, p. 144.

[49] Lemmon, E., Huber, M., and McLinden, M., 2002. "Nist standard reference database 23: Refprop version 9.0". *National Institute of Standards and Technology Boulder, Colorado*, ***80305***.

[50] Bergman, T. L., Incropera, F. P., Lavine, A. S., and DeWitt, D. P., 2011. *Introduction to heat transfer*. John Wiley & Sons.

[51] Kline, S. J., 1953. "Describing uncertainty in single sample experiments". *Mech. Engineering*, ***75***, pp. 3–8.

[52] Moffat, R. J., 1988. "Describing the uncertainties in experimental results". *Experimental thermal and fluid science*, ***1***(1), pp. 3–17.

[53] Test Uncertainty, A., 2006. "Ptc 19.1-2005". *American Society of Mechanical Engineers*, ***3***, pp. 10016–5990.

[54] Harvey, A. H., Bell, I. H., Huber, M. L., Laesecke, A. R., Lemmon, E. W., Meyer, C. W., Muzny, C. D., and Perkins, R. A., 2016. Thermophysical properties of carbon dioxide and co2-rich mixtures. Tech. rep.

[55] Newton, I., 1701. "Scala graduum caloris". *Philos. Trans. Roy. Soc.(London),* **22**, pp. 824–829.

[56] Kays, W., and Crawford, M. "1993, convective heat and mass transfer, mcgraw-hill". *New York.*

[57] Lee, S. H., and Howell, J. R., 1998. "Turbulent developing convective heat transfer in a tube for fluids near the critical point". *International Journal of Heat and Mass Transfer,* ***41***(10), pp. 1205–1218.

[58] Zhao, Z., and Che, D., 2015. "Numerical investigation of conjugate heat transfer to supercritical co2 in a vertical tube-in-tube heat exchanger". *Numerical Heat Transfer, Part A: Applications,* ***67***(8), pp. 857–882.

[59] Kakac, S., 1987. "The effect of temperature-dependent fluid properties on convective heat transfer". *Handbook of Single-Phase Convective Heat Transfer*.

[60] Petrov, N., and Popov, V., 1985. "Heat-transfer and resistance of carbon-dioxide being cooled in the supercritical region". *Thermal Engineering,* ***32***(3), pp. 131–134.

[61] Liao, S., and Zhao, T., 2002. "Measurements of heat transfer coefficients from supercritical carbon dioxide flowing in horizontal mini/micro channels". *J. Heat Transfer,* ***124***(3), pp. 413–420.

[62] Guo, P., Liu, S., Yan, J., Wang, J., and Zhang, Q., 2020. "Experimental study on heat transfer of supercritical co2 flowing in a mini tube under heating conditions". *International Journal of Heat and Mass Transfer,* ***153***, p. 119623.

[63] Krasnoshchekov, E., and Protopopov, V., 1959. "Heat transfer at supercritical region in flow of carbon dioxide and water in tubes". *Therm. Energy,* ***12***, pp. 26–30.

[64] Krasnoshchekov, E., 1966. "Experimental study of heat exchagne in carbon dioxide in the supercritical range at high temperature drops". *High Temperature,* ***4***, pp. 375–382.

[65] Jackson, J., and Fewster, J., 1975. "Forced convection data for supercritical pressure fluids". *Report No. HTFS,* ***21540***.

[66] Jackson, J., 2002. "Consideration of the heat transfer properties of supercritical pressure water in connection with the cooling of advanced nuclear reactors". In The 13th pacific basin nuclear conference. Abstracts.

[67] Mokry, S., Pioro, I., Farah, A., King, K., Gupta, S., Peiman, W., and Kirillov, P., 2011. "Development of supercritical water heat-transfer correlation for vertical bare tubes". *Nuclear Engineering and Design,* ***241***(4), pp. 1126–1136.

[68] Kim, H., Bae, Y. Y., Kim, H. Y., Song, J. H., and Cho, B. H., 2008. "Experimental investigation on the heat transfer characteristics in upward flow of supercritical carbon dioxide". *Nuclear technology,* ***164***(1), pp. 119–129.

[69] Bae, Y.-Y., and Kim, H.-Y., 2009. "Convective heat transfer to co2 at a supercritical pressure flowing vertically upward in tubes and an annular channel". *Experimental Thermal and Fluid Science,* ***33***(2), pp. 329–339.

[70] Kim, D. E., and Kim, M. H., 2010. "Experimental study of the effects of flow acceleration and buoyancy on heat transfer in a supercritical fluid flow in a circular tube". *Nuclear Engineering and Design,* ***240***(10), pp. 3336–3349.

[71] Liu, S., Huang, Y., Liu, G., Wang, J., and Leung, L. K., 2017. "Improvement of buoyancy and acceleration parameters for forced and mixed convective heat transfer to supercritical fluids flowing in vertical tubes". *International Journal of Heat and Mass Transfer,* ***106***, pp. 1144–1156.